Tomographic Imaging of a Two Phase Liquid Metal Flow System

by

BINOD KUMAR

DEPARTMENT OF MECHANICAL ENGINEERING

INDIAN INSTITUTE OF TECHNOLOGY KANPUR

July, 1996

Tomographic Imaging of a Two Phase Liquid Metal Flow System.

A Thesis Submitted

in Partial Fulfillment of the Requirements

for the Degree of

Master of Technology

by

Binod Kumar

to the

DEPARTMENT OF MECHANICAL ENGINEERING

INDIAN INSTITUTE OF TECHNOLOGY, KANPUR

July,1996

CERTIFICATE

Certified that the work contained in the thesis entitled "*Tomographic Imaging of a Two Phase Liquid Metal Flow System.*", by "**Binod Kumar**", has been carried out under my supervision and that this work has not been submitted elsewhere for a degree.

(Dr. P. Munshi)
Associate Professor
Department of Mechanical Engineering,
Indian Institute of Technology,
Kanpur.

July,1996

DEDICATED TO

my

BELOVED PARENTS

ABSTRACT

The liquid-metal magneto-hydrodynamic system has been investigated using methods of computerized tomography. The major experimental effort has been the measurement of the void-fraction distribution across the circular flow area. The convolution-backprojection algorithm has been used to reconstruct void-profiles. Measurements have been carried out for two different halves of the pipe, at two different heights of the pipe, and two different flow rates of nitrogen. The mercury flow rate was monitored by an electromagnetic flowmeter.

The algorithm and programme used has been validated first by doing test runs for approximate Dirac-delta functional (unit pixel) and seven sets of simulated images. The reconstructed void-fraction values have been compared with a previous study. Area-averaged and center-averaged values of void-fraction have been tabulated for both simulated as well as the two-phase liquid-metal flow system. The horizontal centerline plots of reconstructed function, and the plots of error representation, show encouraging results. All the studies have been done for eight different filters and comparison has been done for two Hamming filters, h54(smooth) and h99(sharp).

The results indicate lack of radial symmetry in this mercury-nitrogen pipe flow, and an increase in the void-fraction along the vertical direction.

ACKNOWLEDGEMENTS

The author is deeply grateful to Dr. Prabhat Munshi for his meticulous guidance, invaluable suggestion, constructive criticism and constant encourgement during the tenure of thesis work. It was a great pleasure to work under him as a lot of care with personal touch was rendered. It was under his able guidance that the rudiments of tomography were introduced to me.

The author would also like to thank his teachers for their valuable advices and moral encouragement during the tenure of work.

The author would also be thankful to Mr. S. Yadav, Mr. V. Tomar, Mr. B. Prasad, Mr. Mohsin and Mr. Gopal for their co-operation while working in laboratory.

The author wishes to thank all his friends, in particular Satya,Debashish, MPA, Vishnu, Avi, Ghai, Rathore, Sangeet, Rawat, Nivedan, Manpreet, Bhartendu, Sanjay, Rajesh, Murari, R.P., Rahul, Abhisek, Amod for their cooperation and assistance throught his stay at IIT Kanpur.

Thanks to dear father, mother, brothers, bhabhi and sister whose encouragement led me to complete this postgraduation.

Nomenclature

f	function representing the spatial distribution of any physical quantity
x, y	cartesian co-ordinates
r, ϕ	polar co-ordinates
p	line integral data (projection data)
N	number of photon counts
N_o	initial photon count
μ	absorption coefficient
$\wedge$	Fourier transform
R	Fourier frequency
R_c	cut-off frequency
W	window function
$W''(o)$	second order derivative of window function at zero
E_1	inherent error due to finite cut-off
∇^2	Laplacian
$NMAX$	maximum value of reconstructed grey level
$NMIN$	minimum value of reconstructed grey level
$NRAY$	number of scans per view
$NANGLE$	number of views

List of Tables

List of Figures

Contents

Chapter 1

Introduction

1.1 Image Reconstruction from Projections

The range of applicability of image reconstruction is staggering. At one end data from electron microscope are used to reconstruct the molecular structure of bacteriophages, while at the other end, data collected by rockets sent outside the earth's atmosphere are used to reconstruct the x-ray structure of supernova remnants. Of all the applications, probably the greatest effect on the world at large has been in the area of diagnostic medicine.

Image reconstruction can be very aptly defined in words of Herman (1980) as:

> "Image reconstruction from projections is the process of producing an image of a two-dimensional distribution (usually of some physical property) from estimates of its line integrals along a finite number of lines of known locations".

1.2 An Overview of the Process of CT

The aim of computerised tomography (CT) is to obtain information regarding the nature of the material occupying exact positions inside the object. There are other modes of traditional tomography, e.g., line tomography and transaxial tomography. In traditional forms of tomography, objects which are out of focal plane are visible on the image, although in a blurred form. In CT, the images of cross-sections are not influenced by the objects outside those sections.

1.3 An Overview of the Present Work

In the present study, convolution back projection algorithm (CBP) has been used to study the two phase liquid metal flow system. The data has been collected by Jayakumar(1996a) in the upcomer of the mercury-nitrogen flow in the liquid-metal magneto-hydrodynamic (LMMHD) system, located in the Bhabha Atomic Research Center (BARC). Data is collected using parallel beam geometry. The data has been collected for two halves of the pipe, North half and South half, and two vertical positions, Top and Bottom along the upcomer. Jayakumar et al.(1996b) reconstructed the void fraction using the chord-segment-inversion (CSI) algorithm [Rathore et al.(1988)] which assumes the radial symmetric distribution of void fraction. CBP algorithm requires the data from different views and it does not assume the radial symmetry. The same data has been read repeatedly for different angles to get the required input data. North half and south half form two independent sets of data for CBP algorithm. Using these two sets of data image has been reconstructed and compared.

The computer program developed has been validated by doing test-runs on simulated data from different geometries like circular geometries with holes (simulating pipe and bubbles) and rectangular geometries with a number of holes (simulating

rectangular duct and bubbles), which can resemble a two-phase flow system. The pixel-by-pixel values of absorption coefficient (or void fraction) has been obtained and the reconstructed void fraction value has also been plotted.

1.4 Reconstruction Algorithms

The simplifying assumptions we make in setting up the theory for reconstruction algorithms are:

1. Slices are infinitely thin.

2. For any particular source and detector pair position, all x-ray photons travel in the same straight line (which lies in the infinitely thin slice).

A consequence of the first assumption is that the distinction between the voxel and the pixel disappears. Indeed, since the slice is infinitely thin, it can be thought of as a picture whose gray level at any point (x, y) is proportional to the relative attenuation-coefficient $\mu(x, y)$ at that point. This is the reason why the theory behind reconstruction algorithm is referred to as "*image reconstruction from projections*". Tomographic algorithms can be classified into two categories:

1. Transform methods

2. Series expansion methods

When the set of data available is large and complete, transform methods are generally used. Whereas if the data set is not complete, series expansion methods are preferred. Transform methods are direct methods while series expansion methods can be direct as well as iterative. The scope of the transform algorithm is limited to the reconstruction of a two-dimensional (2-D) image from integrals along a line in the plane, but they are useful in many applications involving three-dimensional

(3-D) objects because such objects can be decomposed into a stack of thin 2-D slices. If line-integral data are available for each of these individual slices independent of others, then the 3-D reconstruction problem may be decomposed into repeated 2-D reconstruction of serial cross-sections of the object.

1.5 Two Phase Liquid Metal Flow System : LMMHD

Since the data used in this work has been collected for two phase liquid metal flow system, the basic operations of magneto-hydrodynamic (MHD) systems with emphasis on the liquid-metal-magneto-hydrodynamic (LMMHD) systems are described briefly in this section. The promise that such systems hold for more efficient generation of electricity and the relevance of void fraction measurements in them are also discussed. The details have been discussed in the article by Satyamurthy (1994) and for convenience it may also be referred briefly from Jayakumar (1996a).

Power converters based on the principles of MHD involve electrodynamic induction caused by a conductor moving across a magnetic field thus inducing an electro motive force. When the conductor is a liquid metal (LM), the system is called LMMHD. The conventional route to produce electrical energy from heat energy requires an intermediate conversion of heat to mechanical work. MHD systems obviate this requirement. MHD systems also eliminate the need of moving parts like turbines etc. This implies considerable improvements in the efficiency and the ease of designing. They also achieve higher thermodynamic efficiency enabling power generation from low-grade heat sources.

1.5.1 Classification

MHD systems can be classified according to the conducting fluid employed in them. Systems using ionised gases (plasma) as the conducting fluid are known as plasma

based MHD converters. Liquid Metal MHD systems use a liquid metal as the conductor.

LMMHD systems can further be classified into gravitational (vertical) and non-gravitational (horizontal) systems. The experimental set-up in which the present void fraction measurements were carried out belongs to the former class.

1.5.2 Gravity Based LMMHD Systems

Fig. (1.1) schematically shows the basic configuration of a gravity based LMMHD system. The principal components of the system are upcomer (U), downcomer (D), mixer (M) and the MHD generator (F). Heat energy is added to the liquid metal by means of a heat exchanger. A vapour, gas, or volatile liquid (called the thermodynamic fluid) is introduced into the mixer at an appropriate pressure and temperature. The two-phase fluid thus created flows to the separator through the the upcomer. The thermodynamic fluid is removed at the separator, condensed, and returned to the mixer. The pressure differential created between the upcomer and downcomer establishes a natural circulation of the liquid metal in the system. A single phase flow of the liquid metal alone takes place in the downcomer and electrical power is extracted from the MHD generator located at its bottom.

1.5.3 Relevance of Void-fraction Measurements in Upcomer

Several parameters are of interest towards the optimisation of the system for a given heat input. These include the total inventory of mercury, flow rates of the electrodynamic and thermodynamic fluids, diameters of the upcomer & downcomer, magnetic field to be applied to the MHD generator etc. It may be noted that many of the parameters above are inter-dependent and a number of studies have been carried out to understand these inter-relationships. Minimisation of the slip between vapour and liquid metal in the upcomer is of crucial importance to achieve maximum liquid

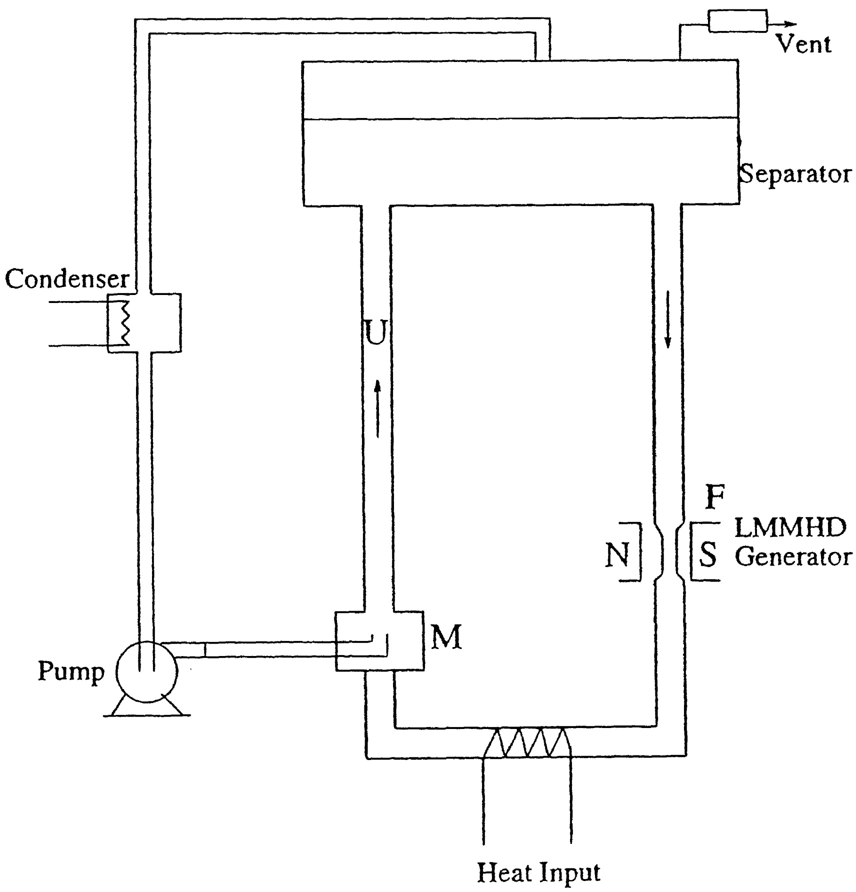

Figure 1.1: Gravity Based LMMHD System

metal flow-rate (& power) for a given heat input. Hence the need to understand the complex two phase flow taking place in the upcomer. The present measurements of void fraction in the upcomer are expected to aid this understanding.

Chapter 2

Theoretical Formulation

In this chapter, the CT related computational and mathematical procedures underlying the data collection, image reconstruction, and image display, are discussed.

2.1 Preliminaries

Number of counts of photon after passing through a thickness dl is given by,

$$N = N_0 e^{-\left(\int_C \mu(r,\phi) dl\right)} \tag{2.1}$$

Here integration is along the chord length,

N = Number of photon counts after passing the chord,

N_0 = Initial photon counts, and

μ = Attenuation coefficient (it depends on the material and energy of the radiation).

Thus,

$$\ln\left(\frac{N_0}{N}\right) = \int_C \mu(r,\phi)dl = p(s.\theta) \quad , \tag{2.2}$$

where $p(s,\theta)$ is called the projection data for the tomographic algorithm, and it is the line integral of function along the line specified by s and θ. (see Fig. 2.1).

Now the aim is to recover the value of $\mu(r,\phi)$, if a set of several p-values measured along various chords is given. This is the fundamental problem of CT and CBP has been used in the present study for that purpose. The μ values can be suitably normalised to get the density values, if so desired.

2.2 Data Collection Mode

The image processing methodology requires attenuation data to be collected by an array of radiation detectors for the reconstruction of the function $\mu(r,\phi)$.

In this study the mode of collections is parallel-beam geometry (PBG) mode (Fig.2.1). This system consists of several pairs of radiation source (S) and radiation detector (D) which can scan the object completely.

The S-D pairs are spaced uniformly and the object can be rotated to get the data for different views. The line SD represents the path of the data ray or the chord along which 'p' value is found out.

The perpendicular distance from the center of the object to the path of ray is denoted by s. Several SD pairs could be used to get the p data. The object table is rotated to get several sets of P for different values of θ.

2.3 The CBP Algorithm

The convolution backprojection (CBP) algorithm has been described in detail by Herman (1980). In this section we review CBP briefly as reported earlier by Munshi(1992).

Fig. 2.1 shows the data collection geometry for a parallel beam CT scanner. The object function, $f(r,\phi)$, is represented by a unit circle and one (of many) data rays is represented by SD. The ray indices are s and θ, where s is the perpendicular distance of the ray from the object center, and θ is the angle of the source position (or object rotation). The CT data is denoted by $p(s,\theta)$ given by,

$$p(s,\theta) = \int_{SD} f(r,\phi)dz \tag{2.3}$$

Here, z is the variable of integration along the chord SD. The CT machine collects the projection data $p(s,\theta)$ for many values of s and θ.

The "Projection-Slice" theorem [Herman(1980)] states the equivalence of the two-dimensional Fourier transform of $f(r,\phi)$ and the 1-dimensional Fourier transform of $p(s,\theta)$ with respect to s. Symbolically,

$$\hat{p}(R,\theta) = \hat{f}(R\cos\theta, R\sin\theta) \tag{2.4}$$

where, the symbol $\wedge$ represents the Fourier transform and R is the Fourier frequency.

A two-dimensional Fourier inversion of Eq.(2.4) leads to the well known tomographic inversion formula,

$$f(r,\phi) = \int_0^\pi \int_{-\infty}^{\infty} \hat{p}(R,\theta)e^{i2\pi Rr\cos(\theta-\phi)}|R|dRd\theta \tag{2.5}$$

where,

$$\hat{p}(R,\theta) = \int_{-\infty}^{\infty} p(s,\theta)e^{-i2\pi Rs}ds. \tag{2.6}$$

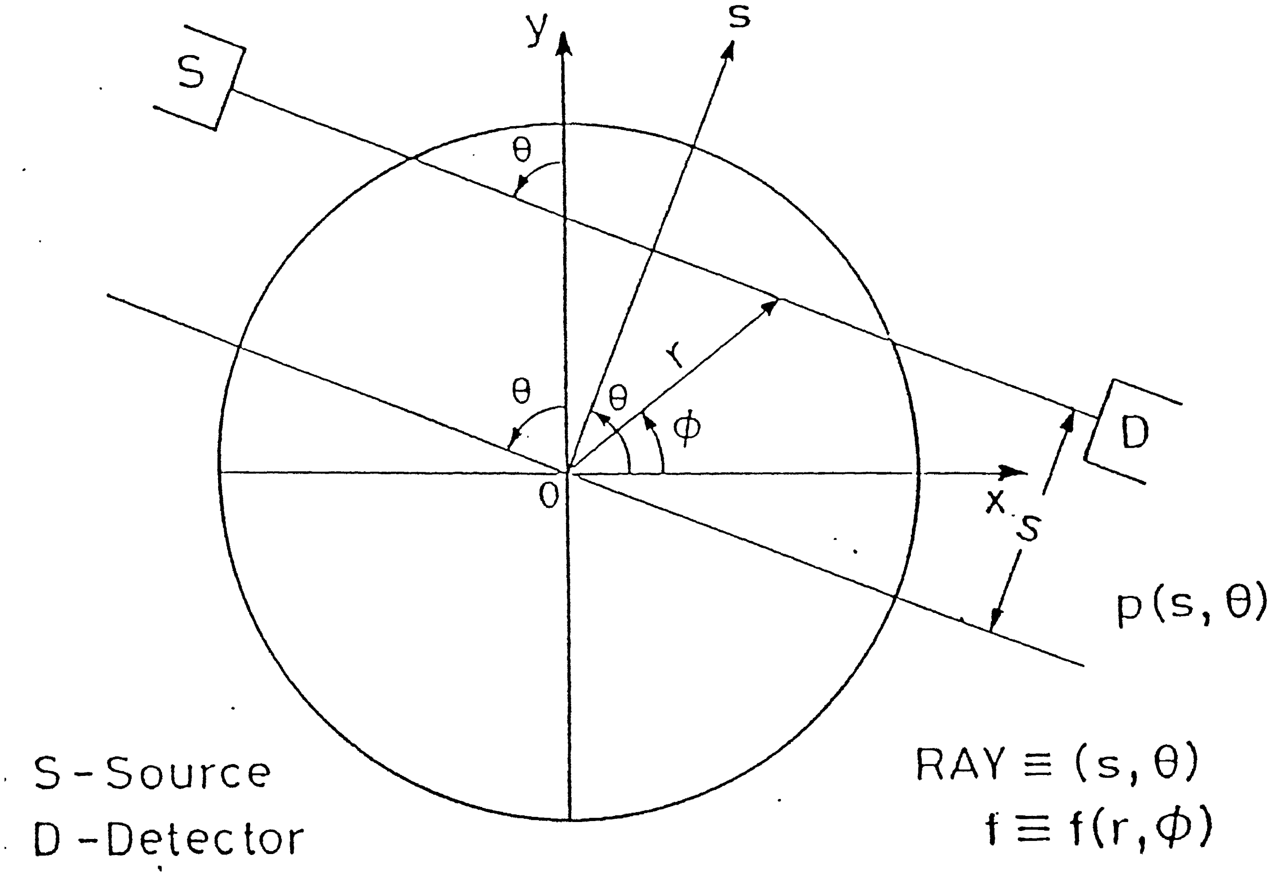

Figure 2.1: Data Collection Geometry

We note that the inner integral in Eq.(2.5) is divergent. A practical implementation of Eq.(2.5) incorporates the replacement of the factor $|R|$ by $|R|W(R)$, where $W(R)$ is a suitable window function which vanishes outside the interval $[-R_c, R_c]$. Here $|R_c|$ is the Fourier cut-off frequency. Normally, $W(R)$ is an even function of R. Thus Eq.(2.5) takes the approximate form,

$$\tilde{f}(r,\phi) \approx \int_0^{\pi} \int_{-\infty}^{\infty} \hat{p}(R,\theta) e^{i2\pi Rr\cos(\theta-\phi)} |R| W(R) dR d\theta \tag{2.7}$$

If $\hat{p}(R,\theta)$ also vanishes for $|R| > R_c$, then the reconstructed f, denoted by $\tilde{f}$, agrees exactly with f the following window,

$$W(R) = \begin{cases} 1 \ , & |R| \ \leq \ R_c \\ 0 \ , & |R| \ > \ R_c \end{cases} \tag{2.8}$$

An implementation of Eq.(2.7) in the spatial domain exploits the convolution theorem of Fourier transform so that the reconstruction, $\tilde{f}$, is given by,

$$\tilde{f}(r,\phi) \approx \int_0^{\pi} \int_{-\infty}^{\infty} p(s,\theta) q(s'-s) ds d\theta \tag{2.9}$$

where,

$$q(s) = \int_{-\infty}^{\infty} |R| W(R) e^{i2\pi Rs} dR \tag{2.10}$$

and,

$$s' = r\cos(\theta - \phi) \tag{2.11}$$

The index s' is of the data ray passing through (r,ϕ), the point being reconstructed. The inner integral in Eq.(2.9) is a 1-dimensional convolution, and the outer integral (corresponding to the averaging operation over θ) is termed as backprojection, and hence, the name convolution backprojection for this particular implementation. The CBP method is also known as the filtered backprojection algorithm due to the 'filtering' of the Fourier transform of the projection data, $\hat{p}$, by the window (or filter) W(R) in the initial stages of formulation as given by Eq.(2.7). The function q(s), known as the convolving function, is evaluated once and stored for repeated use for different views (or different angles θ). So, for a given point (r,ϕ), the inherent

error E_1, in the CBP implementation, Eq.(2.9) is,

$$E_1(r,\phi) = f(r,\phi) - \tilde{f}(r,\phi) \tag{2.12}$$

where f and $\tilde{f}$ are given by Eq.(2.5) and Eq.(2.7) respectively. This error is strictly due to finite cut-off, R_c, of the Fourier frequency and is precisely zero if the projection data happens to be band-limited and the cut-off frequency is chosen to be the highest frequency contained in $\hat{p}$. In general, to avoid aliasing artifacts [Herman(1980)], it is recommended to choose,

$$R_c = 1/(2\Delta s) \quad ,$$

where Δs is the spacing of the data rays.

It has been shown [Munshi(1992)] that E_1 at a given point (r,ϕ) in the object cross-section, is given by,

$$E_1(r,\phi) \approx k(W''(0))(\nabla^2 f(r,\phi)) \tag{2.13}$$

where,

$$W''(0) = \left.\frac{\partial^2 W(R)}{\partial R^2}\right|_{R=0} \tag{2.14}$$

and $\nabla^2 f$ is the Laplacian of f,

and, K is a constant depending on the data-ray spacing. Eq.(2.13) is valid for objects having certain smoothness properties provided the data is perfect as per Eq.(2.3).

The error E_1 represents the point-wise theoretical error in reconstruction, and it also obvious that the Laplacian of $f(r,\phi)$ has to exist for the predictions of the theorem to be valid. For points in the cross section, where $\nabla^2 f$ does not exist, the linearity between E_1 and $W''(0)$ is disturbed. If $\nabla^2 f$ is zero, or near zero, other errors will be more dominant. The Laplacian is zero for smooth regions of the

objects, while it does not exist for rough edges. For simulated objects, E_1 can be calculated from the original image, but for real objects the distribution is unknown, hence the error in reconstruction cannot be calculated directly. This fact motivates and indirect representation of error. It has been reported earlier that, for a given data set, sharpness can be used as an indicator of the behaviour of error, arising due to the choice of the filter function.

If the image consists of a single point then the sharpness parameter is defined as the value of the reconstructed grey level at that point. For a general image, the sharpness parameter corresponds to, NMAX, the maximum grey level (linear absorption coefficient) in the reconstruction.

In the present work $1/NMAX$ (inverse of sharpness) along with Eq.(2.13) has been used to represent the physical nature of the object cross section.

Chapter 3

Programme

3.1 Numerical Implementation of the Programme for Discrete data

In practical application of reconstruction from projections, the measured data correspond to the estimates of $p(s, \theta)$ for numerous values of s and θ. And the aim is to find the function $\mu(r, \phi)$.

Further, for the simplification of the reconstruction algorithm the projections are sampled uniformly in both s and θ. Therefore, for each view there are M equi-spaced rays Δs apart, and N such views $\Delta\theta$ apart. We thus define:

$$\left.\begin{aligned} M^{+} &= (M-1)/2 \\ M^{-} &= -(M-1)/2 \end{aligned}\right\} \text{For odd M}$$

$$\left.\begin{aligned} M^{+} &= (M/2) \\ M^{-} &= -(M/2) \end{aligned}\right\} \text{For even M}$$

In order to ensure that the collection of rays specified by

$$\{(m\Delta S, n\Delta\theta) : M^{-} \leq m \leq M^{+}, 1 \leq n \leq N\}$$

covers the unit circle from a complete range of directions, we choose

$$\Delta\theta = \pi/N,$$

and
$$\Delta S = 1/M^{+}$$

3.2 Programme for Simulating Data

The simulated data has been generated for the following cases:

1. Unit circle
2. Unit circle with a hole of 0.3 unit radius.
3. Annular hole in the unit circle.
4. Rectangular cross-section with two holes: One at the geometric center and the other off-centered hole.
5. Rectangular cross-section with four holes at symmetrical positions at four corners.
6. Rectangular cross-section with nine holes of different sizes at different locations.
7. Rectangular cross-section with a rectangular hole at the center and fur holes spread symmetrically.

The number of rays, NRAY and the number of views, NANGLE can be varied as per the need. The programme written is a general one. For circular geometries, the region has been divided into three sectors of radius r_1, r_2, r_3 and absorption coefficient f_1, f_2, f_3 respectively. For rectangular geometry also the programme will work for any number of holes. Subroutine 'h' finds the path-length of the ray lying

in the circular (hole) region and the subroutine 'length' does the same for the rectangular region.

3.3 Programme for Reconstruction

The convolution backprojection algorithm uses the data of parallel beam geometry to reconstruct the image of a cross-section.

The projection data has been kept in the input file "PRO21.DAT". It writes the reconstructed CT numbers in "RES.DAT" file which, beside CT numbers also contain maximum, minimum, cross-sectionally averaged and centerline averaged LITF values. The LITF values along the horizontal center line is stored in a file called PLOTF to get the plot of absorption coefficient 'vs' NRAY. In the present work eight filters have been used to study the tomographic image. Beside the Ramachandran-Lakshminarayan filter (Ram-Lak), sine, cosine and five Hamming filters have been used. They are given by :

$$W(R) = \begin{cases} 1 & Ram - Lak \\ \frac{sin(\pi R/2R_c)}{\pi R/2R_c} & Sin \\ cos(\pi R/R_c) & Cos \\ B + (1-B)\cos(\pi R/R_c) & Hamming \end{cases} \tag{3.1}$$

The details of the filters are listed in Table 3.1 with their Fourier-Space origin second derivatives, $|W''(0)|$.

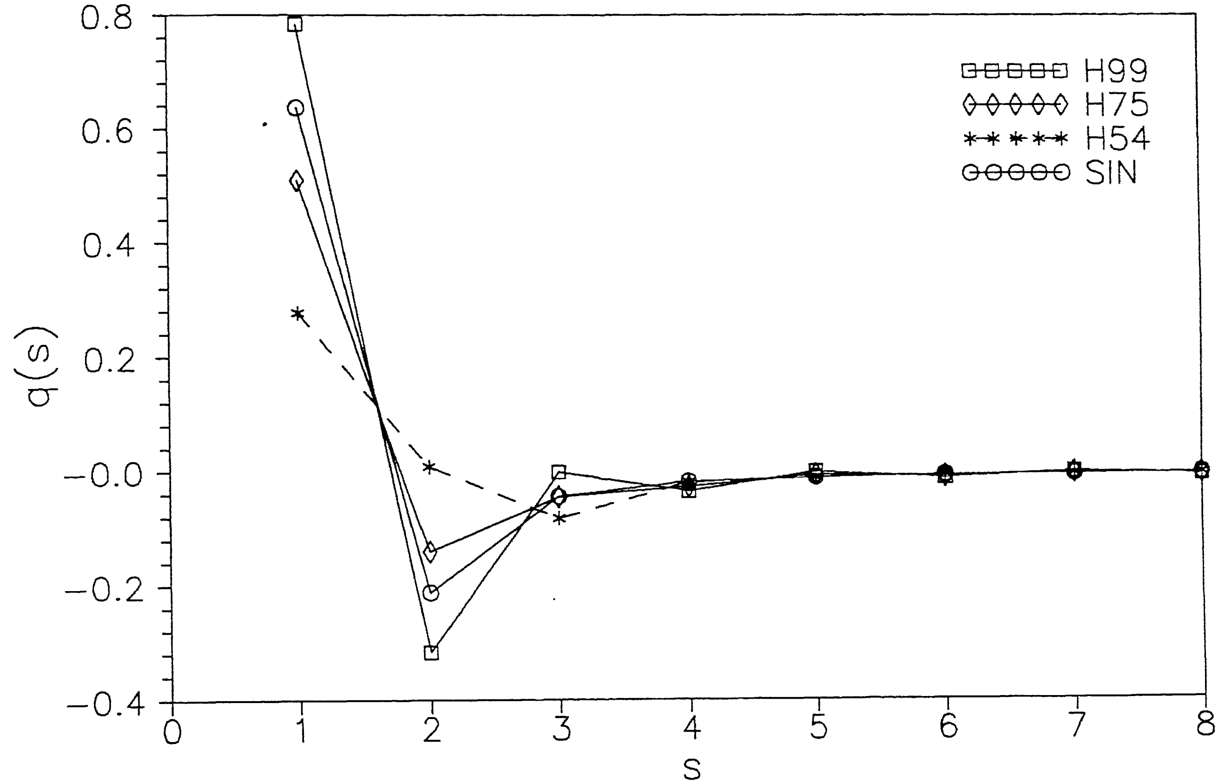

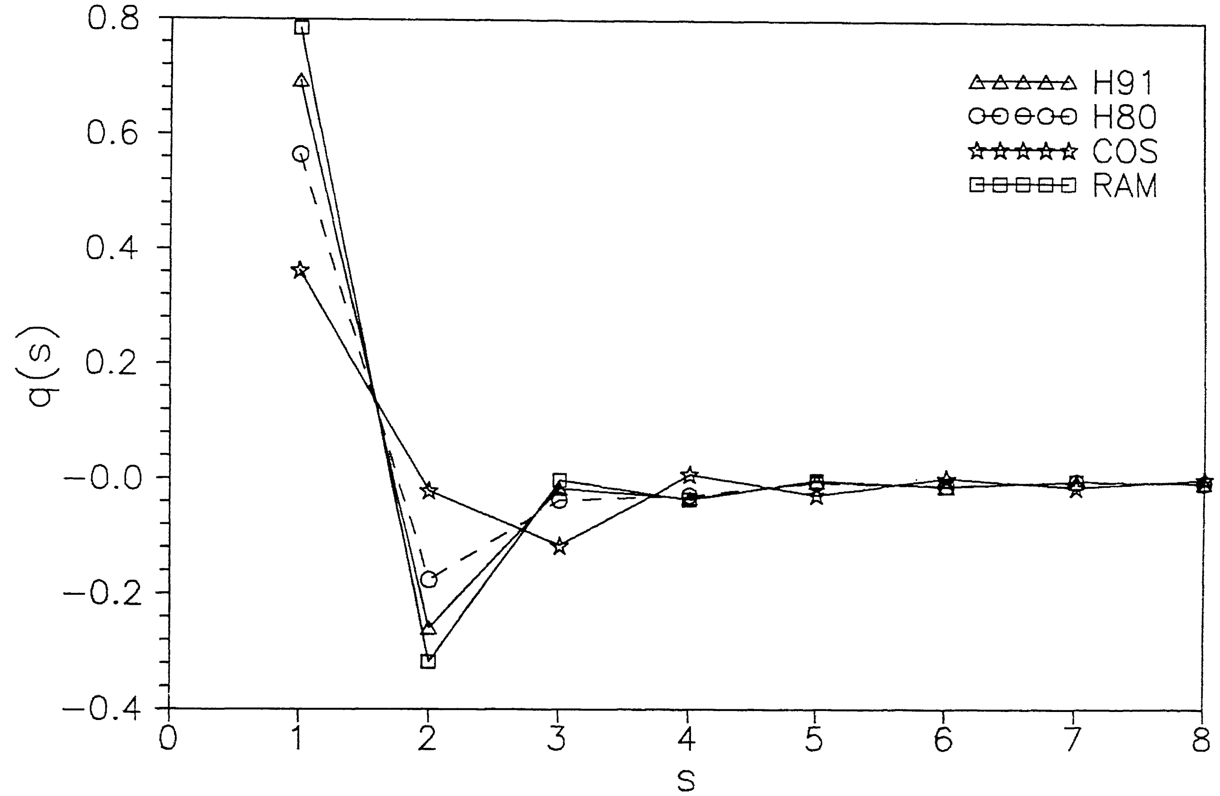

Fig. 3.1: Plot of Filter Coefficients

Filter code	B	$\|W''(0)\|$
Ram-Lak	–	0.000
Sin	–	0.083
cos	–	0.250
h99	0.999	0.001
h91	0.917	0.083
h80	0.800	0.200
h75	0.750	0.250
h54	0.540	0.460

Table 3.1: Details of Hamming Filters selected

3.4 Programme for Displaying Reconstructed Image and Gray Levels

For the purpose of displaying the image, the CT numbers from the file "RES.DAT" is read and appropriate gray levels assigned corresponding to that. At the position of each number a small rectangle is drawn and filled with gray level corresponding to that CT number. The image produced is a pixel. Thus by generating pixels for each CT numbers at their positions they can be graphically displayed. The colour code is printed adjacent to it for quick reference.

3.5 Colour Code

The colour code is a must to understand and extract information from the coloured images produced in the present work. The natural choice for the colour code was our own solar spectrum "VIBGYOR" in the scale of 0 to 100. Number 0 is represented by 'Violet' and 100 by 'Red' and the intermediate colours linearly interpolated to represent other numbers.

Chapter 4

Details of Data Collected

Void-fraction profile measurements in a liquid metal two phase (mercury-nitrogen) flow were carried out in the upcomer of the LMMHD system by Jayakumar(1996). This experimental set-up is situated at the Laser & Plasma Technology Division of Bhabha Atomic Research Center (BARC). The salient features of the gamma-densitometer are given in Table 4.1.

4.1 Flow system

A schematic diagram of the LMMHD setup is shown in the Fig. 4.1. Void fraction measurements were carried out at two elevations of the upcomer (U), 1.1 m and 2.8 m above the mixer (M). The upcomer is a 4.06 m long stainless steel pipe, 77.9 mm inner diameter and 5.5 mm thick.

The required inventory of mercury is loaded into the system from the accumulator (A). Mercury is circulated in the loop by admitting nitrogen from a bank of cylinders at the bottom of the upcomer through the mixer.

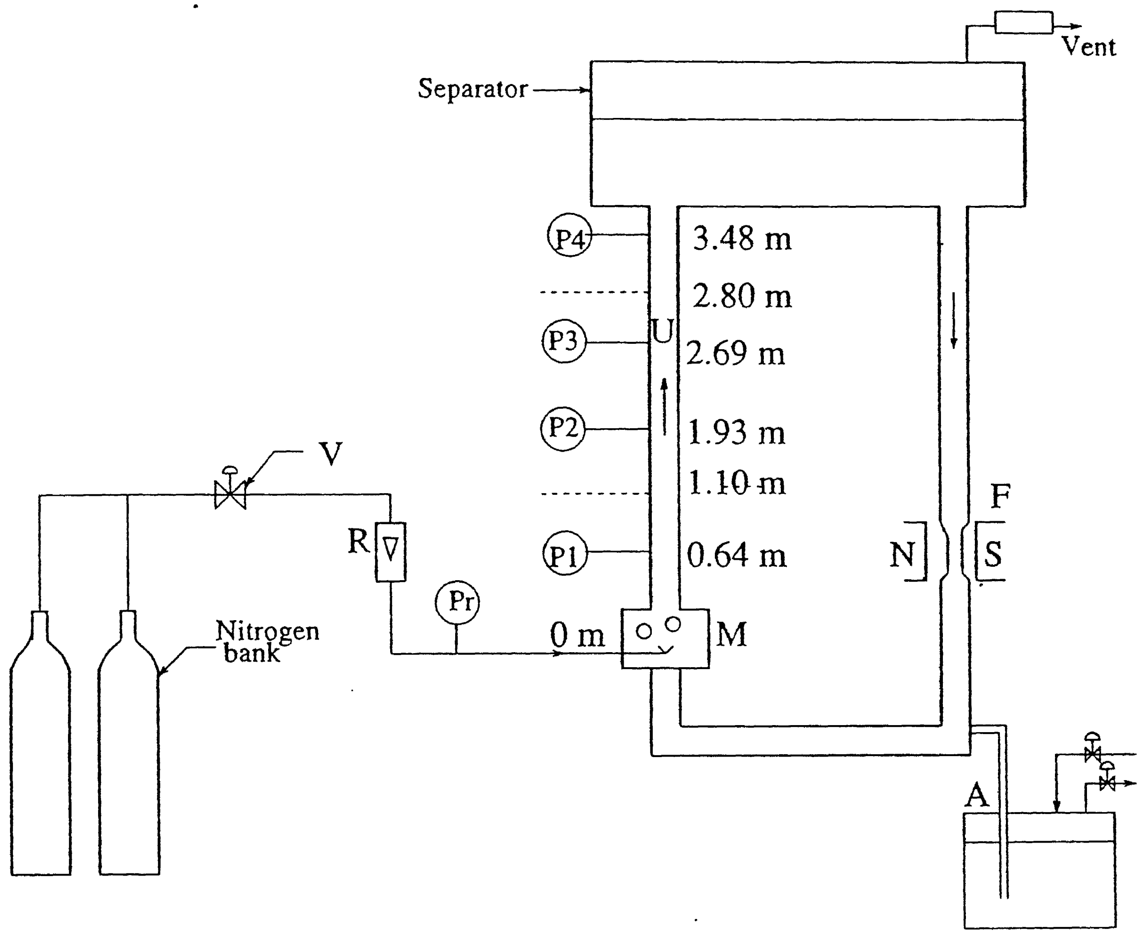

U - Upcomer, M - Mixer, A - Accumulator, F - MHD flow meter, V - Nitrogen inlet valve, R - Rotameter.

Figure 4.1: Flow System

Sl. No.	Item	Details
1	Pipe	Dimensions - 88.9 mm OD x 77.9 mm ID Material - Stainless Steel
2	Gamma-ray Source	Co-60 Strength - 20 mCi
3	Collimation	By means of 3 mm dia holes in 50 mm tk. lead blocks. Both at source-end & detector-end
4	Detector	NaI(Tl) Scintillation head.
5	Signal processing Instrumentation	Operating in count-mode with the SCA set to detect 1.33 MeV. Window = 40 eV.
6	Data collection Geometry	Parallel-beam mode. ray spacing in scans = 2 mm(min),7mm(max)

Table 4.1: Densitometer Details

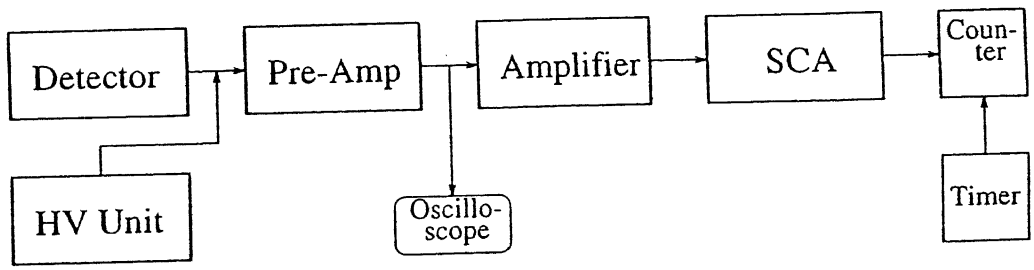

Figure 4.2: Signal Processing Instrumentation

4.2 What Forms The Data

Following Jayakumar(1996), a summary of the input data is presented for convenience.

To determine void fraction distribution at a certain plane, length averaged void fractions along a number of parallel chords at different radial distances between the centre and inner periphery of the pipe are to be obtained. These form the input to the algorithms of Chapter 2. The length-averaged void fraction along a chord is calculated. Therefore, through any chord, characterised by its perpendicular distance from the centre of the pipe, three count rates are to be measured with the following media filling the pipe:

1. Nitrogen (or air)
2. Mercury
3. Mercury-nitrogen two phase flow, of a fixed nitrogen flow rate.

We refer to a *reading* as the number of counts observed and the time taken to do so. A set of readings taken along a number of parallel chords from the centre to the inner periphery of the pipe is referred to as a *scan*. For a given nitrogen flow rate, the two phase, mercury and air scans together form the *data* for that flow rate, with the readings of these scans taken along exactly the same chords. That is, the data for two different flow rates at a given plane and half of the pipe differ only in their two-phase flow scans.

4.3 Data Collected

The experiment was carried out at two elevations of the upcomer, at 1.1 m (bottom) and 2.8 m (top) above the mixer. At each elevation scanning was done on both (north & south) halves.

Cases	Nitrogen flow rate (lpm)	Elevation	Half	No. of readings per scan	NRAY
BN600	60	Bottom	North	19	37
BS600	60	Bottom	South	19	37
BS400	40	Bottom	South	19	37
TS400	40	Top	South	19	37
BN400	40	Bottom	North	10	19
TN400	40	Top	North	10	19
TN600	60	Top	North	10	19
TS600	60	Top	South	10	19

Table 4.2: Parameters for LMMHD data sets

Following the recommendation of Munshi and Vaidya (1994) a minimum of 3000 photon counts were collected for each two phase and mercury readings. For air readings this minimum ranged between 7000 and 15000 for different data-sets.

The data are represented as 8 cases depending upon the following:

1. Elevation (top or bottom)
2. Half (north or south)
3. Nitrogen flow rate (40 or 60 liters per minute)

The name assigned to the eight cases along with related parameters appear in the Table 4.2. Since the data collected by Jayakumar(1996) is assumed to be inherently radially symmetric and collected for one half only. it has been rolled over to get the complete datasets. Thus,

$$NRAY = (2\times \text{ No. of readings per scan}) - 1$$

Chapter 5

Validation of the CBP Programme

In this chapter, the results obtained from simulated data has been presented. The results obtained from simulated data have validated the programme used for CBP.

Key to Photographs

In the photographs various types of relevant information has been displayed. The filter name appears with the ".fil" extension. In case of simulated data, the actual object appears on the bottom-right hand corner whereas the reconstructed image appears on the top-left hand corner. Relevant information has been displayed on the top-right hand corner. The symbols are explained below.

C_0	:	grey level corresponding to violet (0 on 0 to 99 scale)
C_99	:	grey level corresponding to red (99 on 0 to 99 scale)
NMAX	:	maximum value of grey level
NMIN	:	minimum value of grey level
A-AVG	:	cross-sectionally averaged value of grey level
C-AVG	:	average value of grey levels along the horizontal centerline

The colour code bar is given on the top of the photograph from violet to red (0 to

99). To get grey level corresponding to a colour, it has to be linearly interpolated between two ends.

5.1 Approximate Dirac-delta function(Unit Pixel)

Dirac-delta functional is the ideal test set for validating the error theorem [Eq.(2.13)] and the use of sharpness (in this case inverse of sharpness or NMAX) for representing error [Munshi et al.(1993)]. Error analysis has been done in chapter 7. Results for Dirac-delta functional have been tabulated in Table 5.1.

Filters	A-AVG	C-AVG	NMIN	NMAX	$1/NMAX$
h54	0.0142	0.2579	-0.0248	5.0006	0.200
h75	0.0154	0.3629	-0.03335	9.1687	0.109
h80	0.0156	0.3879	-0.0400	10.1612	0.098
h91	0.0163	0.4465	-0.0554	12.4839	0.080
h99	0.0167	0.4875	-0.2459	14.1116	0.071
sine	0.0159	0.4233	-0.0434	11.44574	0.087
cosine	0.0144	0.3035	-0.1497	6.5404	0.153
Ram-Lak	0.0167	0.4880	-0.2488	14.1315	0.071

Table 5.1: Summary of results of approximate Dirac-delta functional for different filters

The reconstruction of the approximate Dirac-delta functional has been shown in Fig. 5.1 for two of the hamming filters: h54 and h99. The plot of horizontal centerline grey level is shown in Fig. 5.2. By looking at the Fig. 5.2 the smoothing effect of h54 is evident. NMAX value in case of h99 is 14.1116 as compared to 5.0006 in case of h54. Also the A-AVG value are also different for two filters. Refer to Table 5.1 for values corresponding to other filters.

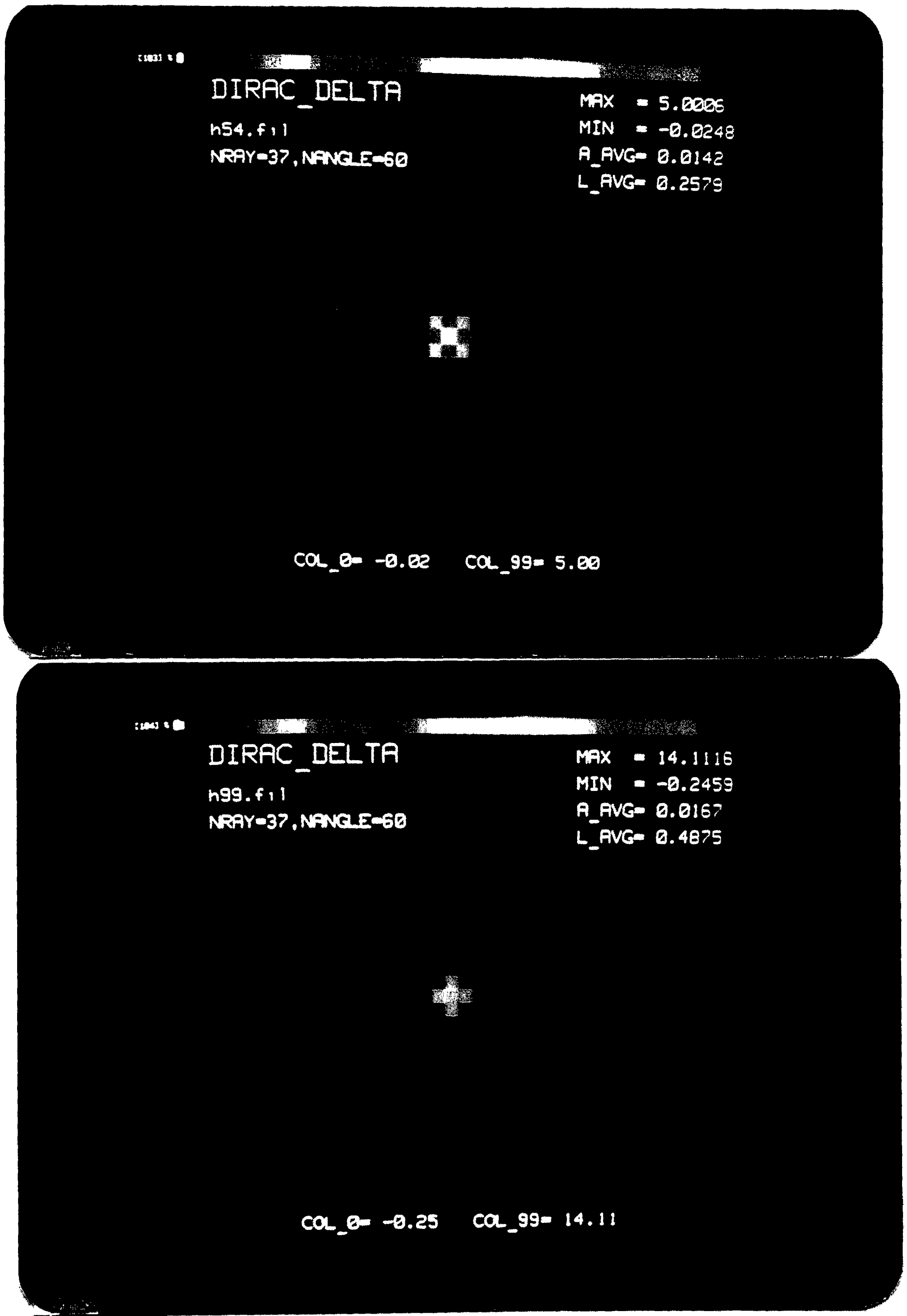

Figure 5.1: Reconstruction of Unit Pixel (a)for **h54** and (b)for **h99**

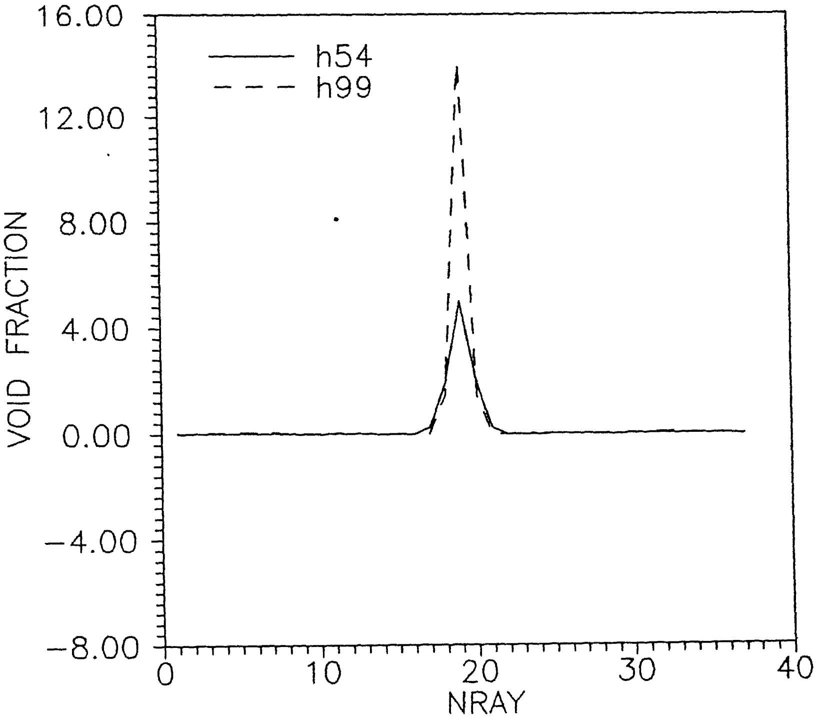

Fig. 5.2 : Plot of Horizontal Centerline values for Dirac–Delta functional

5.2 Validation from Simulated Data

The simulated data have been studied for seven samples as mentioned in section (3.2). The results have been summarised in Table 5.2.

The reconstructions are shown in Figs. 5.3-5.9. Reconstruction has been done for h54 and h99 filters. Image due to h54 is labelled as "a" and that due to h99 as "b". Thus Fig. 5.3(a) is the reconstruction due to h54 filter and Fig. 5.3(b) due to h99 filter of sample 1. Unit circle is easiest to reconstruct and gives the most accurate reconstruction. The photographs are self explanatory with the help of *Key to Photographs* given at the beginning of this chapter. Sample 2 and 3 has been chosen to represent the two phase flow system. Other samples show the reconstruction for increasingly complex geometry. The filter h99 is sharp, hence it

	NMAX		NMIN		A-AVG		C-AVG	
Sample	h54	h99	h54	h99	h54	h99	h54	h99
S1	1.0531	1.1798	0.00	0.00	0.8241	0.8068	0.9707	0.9727
S2	1.0523	1.1836	0.00	0.00	0.7538	0.7363	0.6818	0.6817
S3	1.0557	1.1908	0.00	-0.021	0.5125	0.4957	0.5792	0.5823
S4	1.0358	1.0757	-0.057	-0.213	0.3926	0.3917	0.3965	0.3927
S5	1.0606	1.0963	-0.054	-0.195	0.4044	0.4030	0.6548	0.6532
S6	1.0657	1.1095	-0.074	-0.238	0.3401	0.3389	0.3289	0.2940
S7	1.0619	1.1124	-0.055	-0.213	0.3323	0.3310	0.3931	0.3917

Table 5.2: Summary of results for simulated data for h54 and h99 filters

as compared to h54 filter (compare Fig. 5.8(a) and Fig. 5.8(b)).

By looking at the reconstructed functions (plots) and images, we conclude that the results obtained are good. The quality of reconstruction of simulated objects are very good because of absence of any error but the error in the CBP algorithm. The gray level distribution is symmetrical for symmetrical objects.

The gray level do not sharply change at edges as in the actual objects. Thus the **Edge Effects** are visible. But the density of reconstructed section of simulated data is uniform at 4 to 6 pixel away from the edge or the boundary.

To study the edge effects at locations other than the center. We have reconstructed the image of rectangular objects with the off-centered holes. The results are very encouraging. It shows that CBP algorithm can also give pretty good reconstructions of circles at off-centered positions,too.

Figs. 5.10-5.16 show the horizontal centerline plot for simulated data. For circularly symmetric objects (S1 to S3) it is same for any radial line but for other samples (S4 to S7) horizontal centerline value does not show all the details.

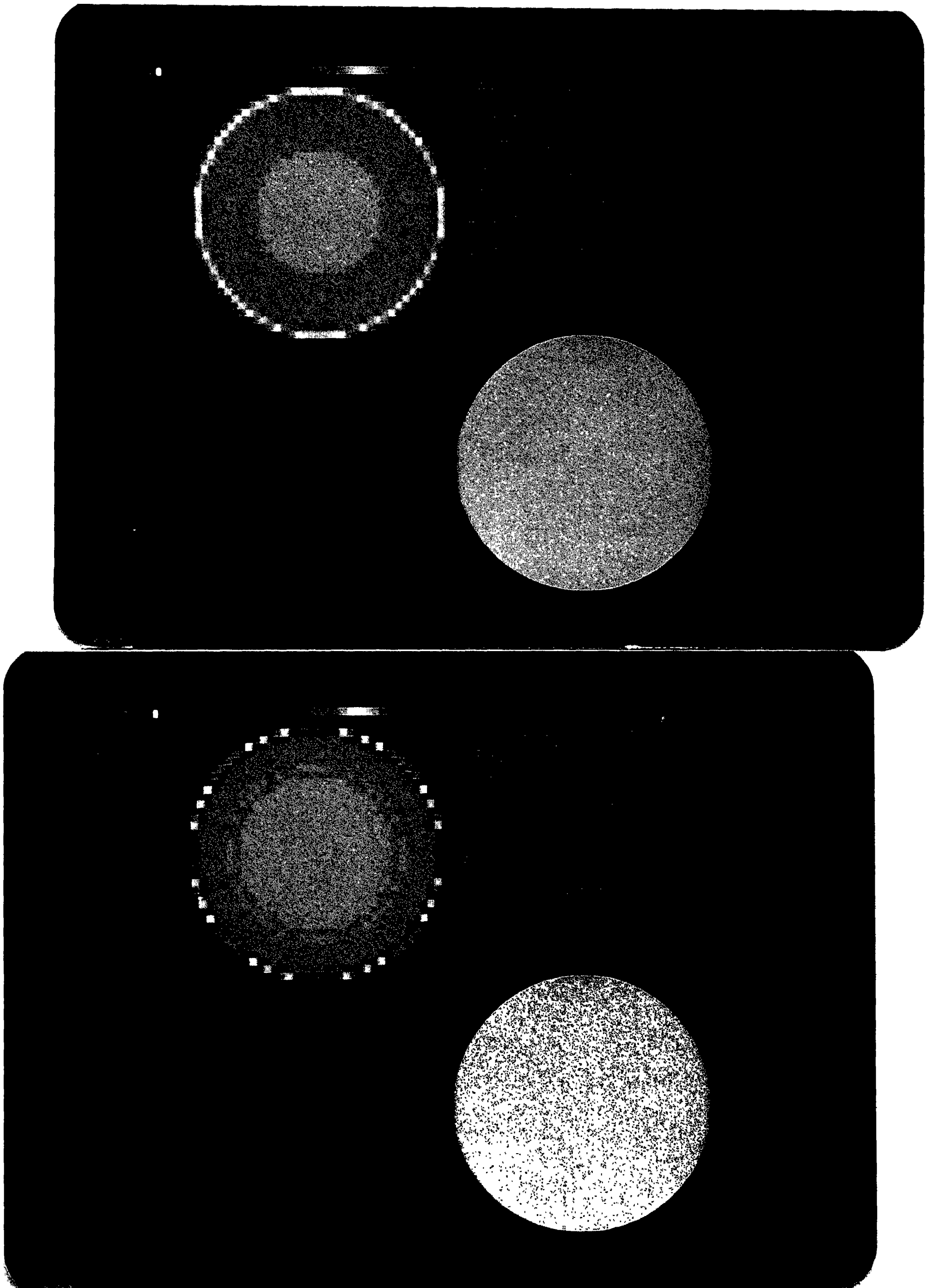

Figure 5.3: Reconstruction of Sample 1 (a)for **h54** and (b) for **h99**

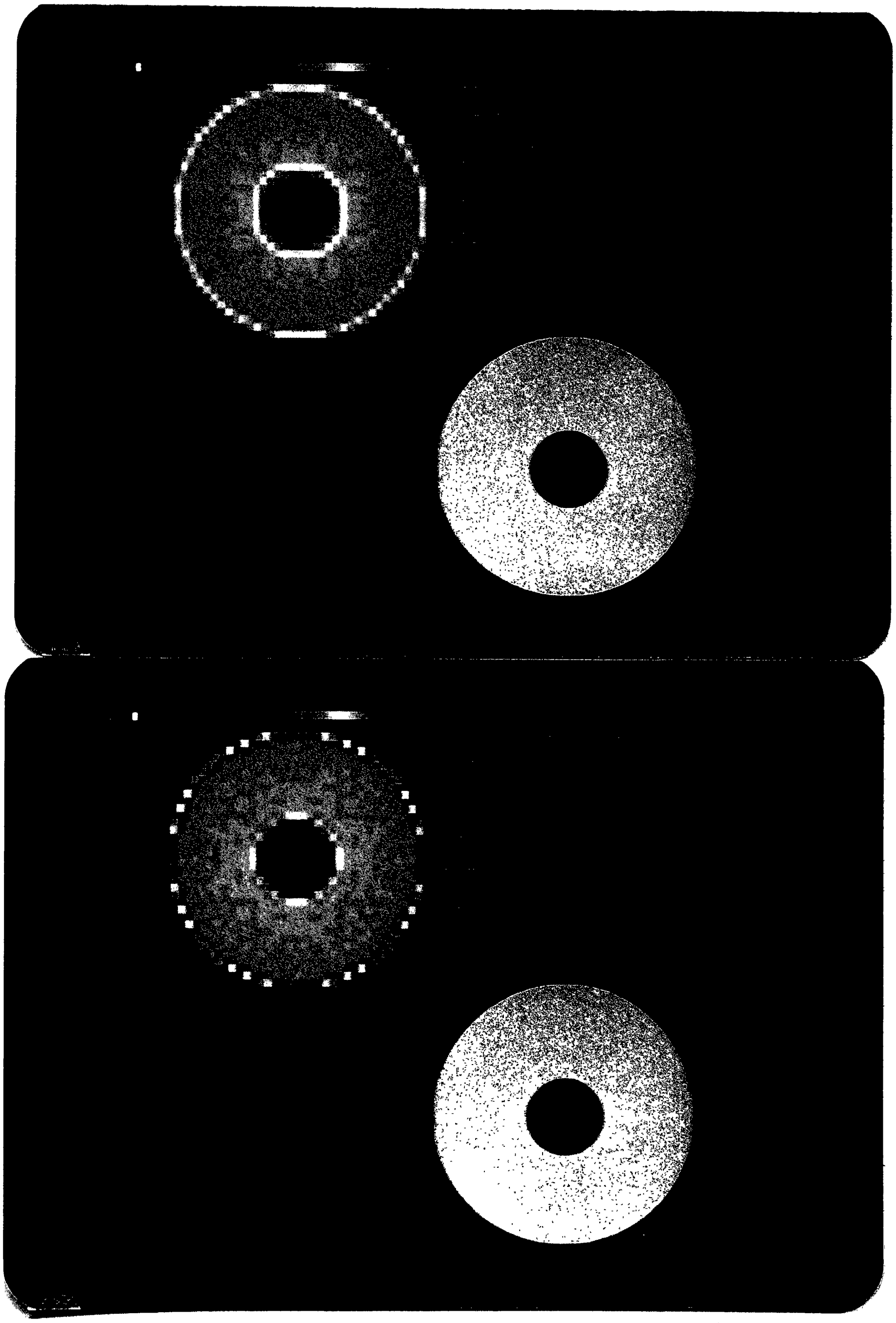

Figure 5.4: Reconstruction of Sample 2 (a)for **h54** and (b) for **h99**

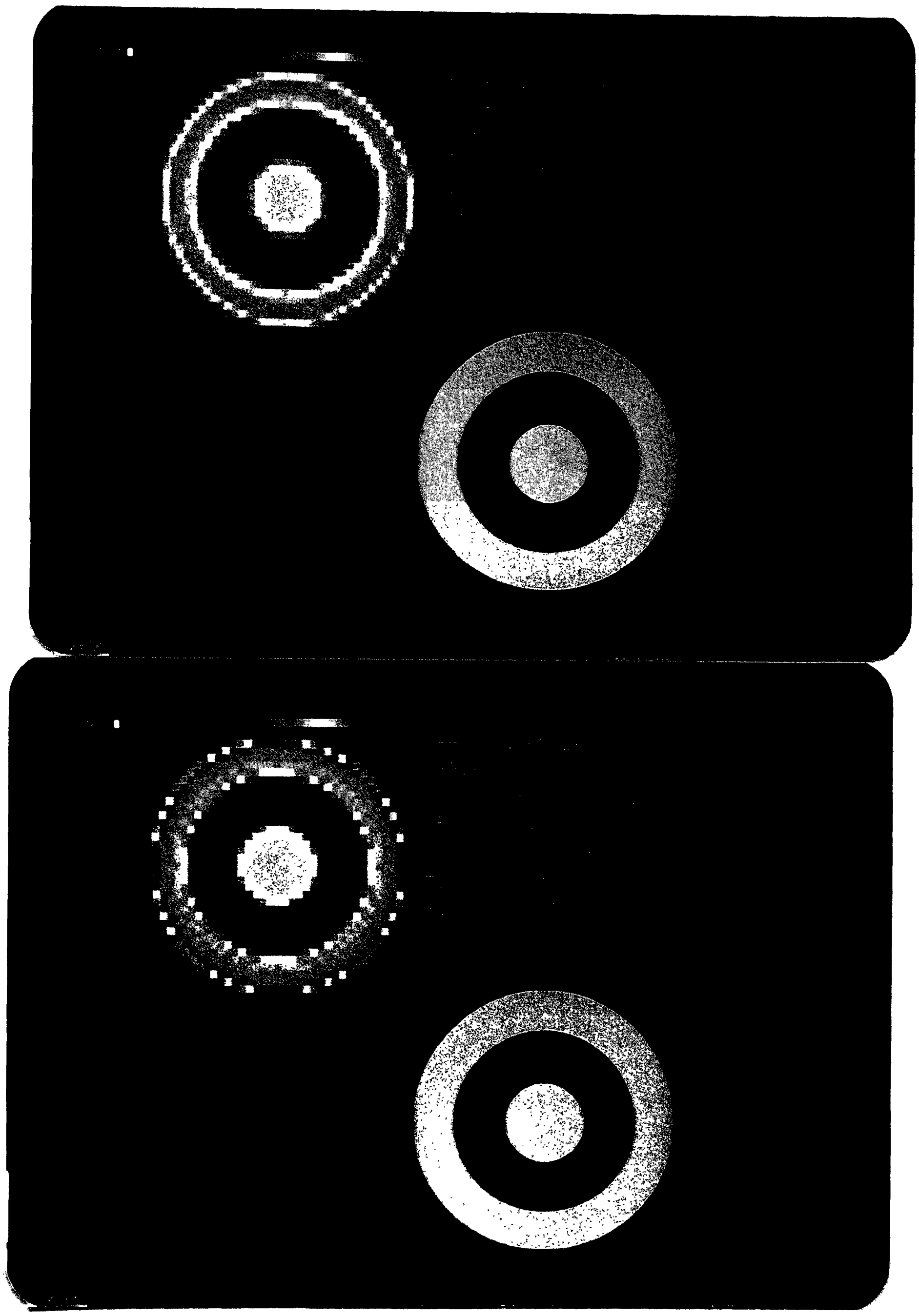

Figure 5.5: Reconstruction of Sample 3 (a)for **h54** and (b) for **h99**

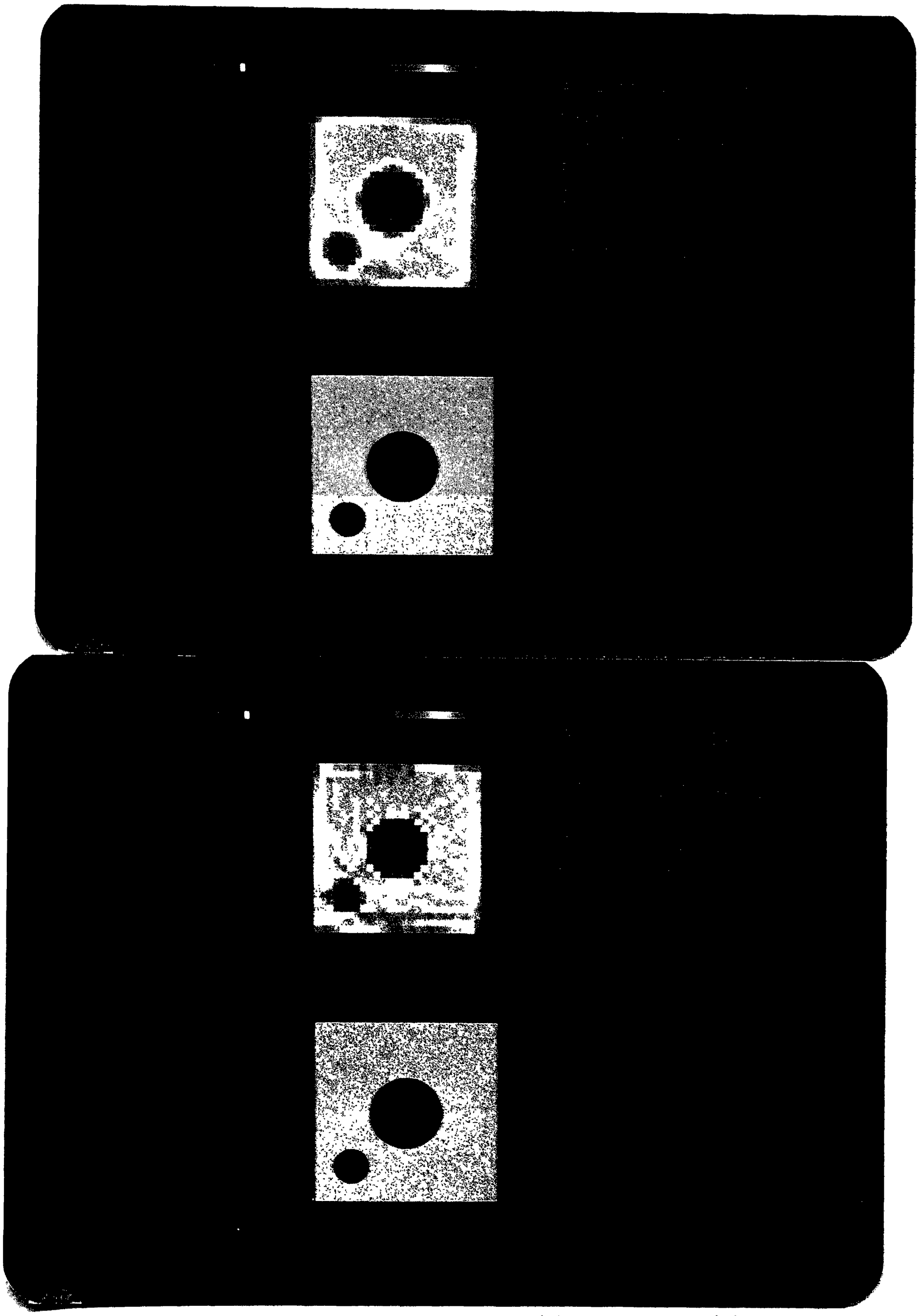

Figure 5.6: Reconstruction of Sample 4 (a)for **h54** and (b) for **h99**

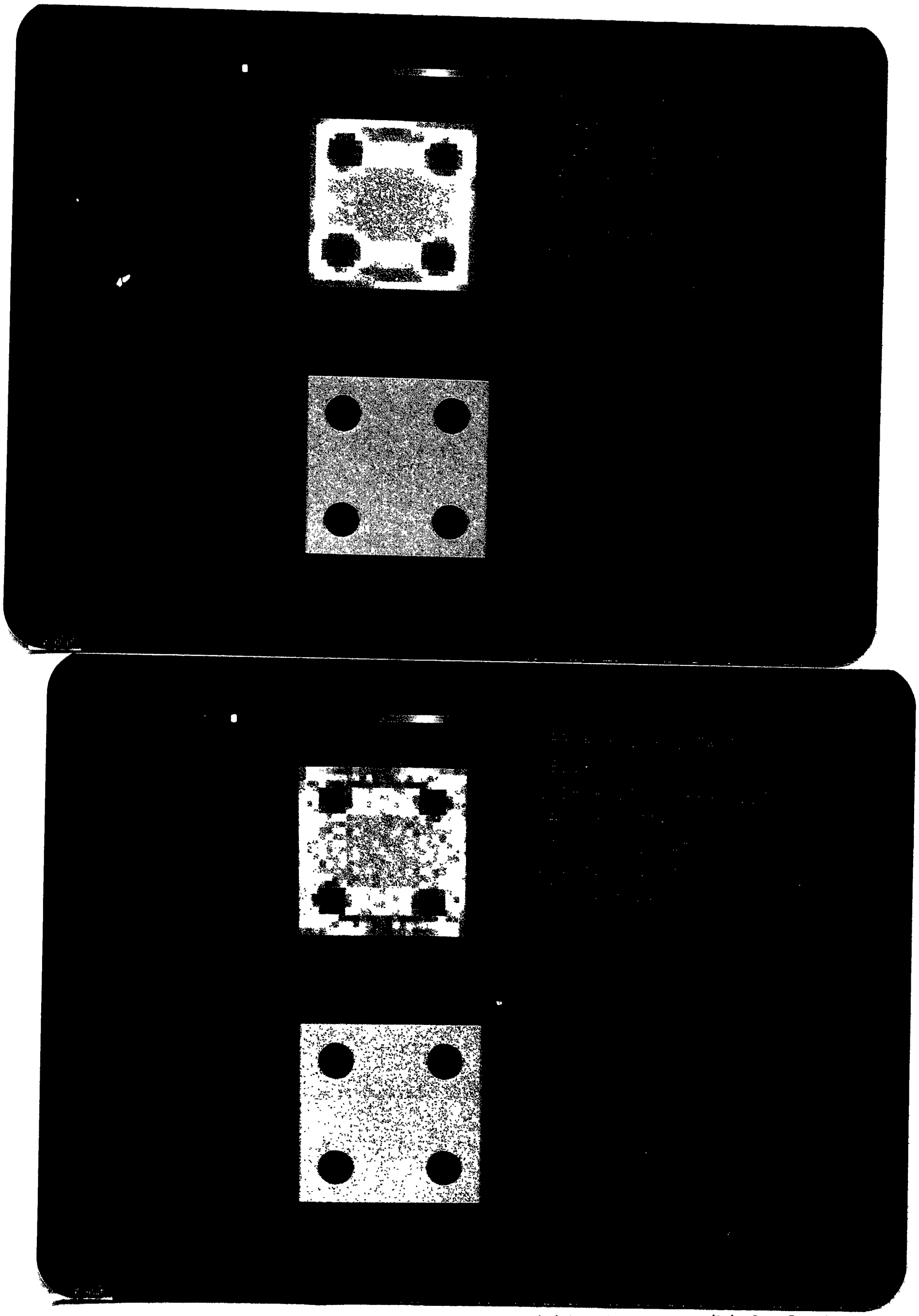

Figure 5.7: Reconstruction of Sample 5 (a)for **h54** and (b) for **h99**

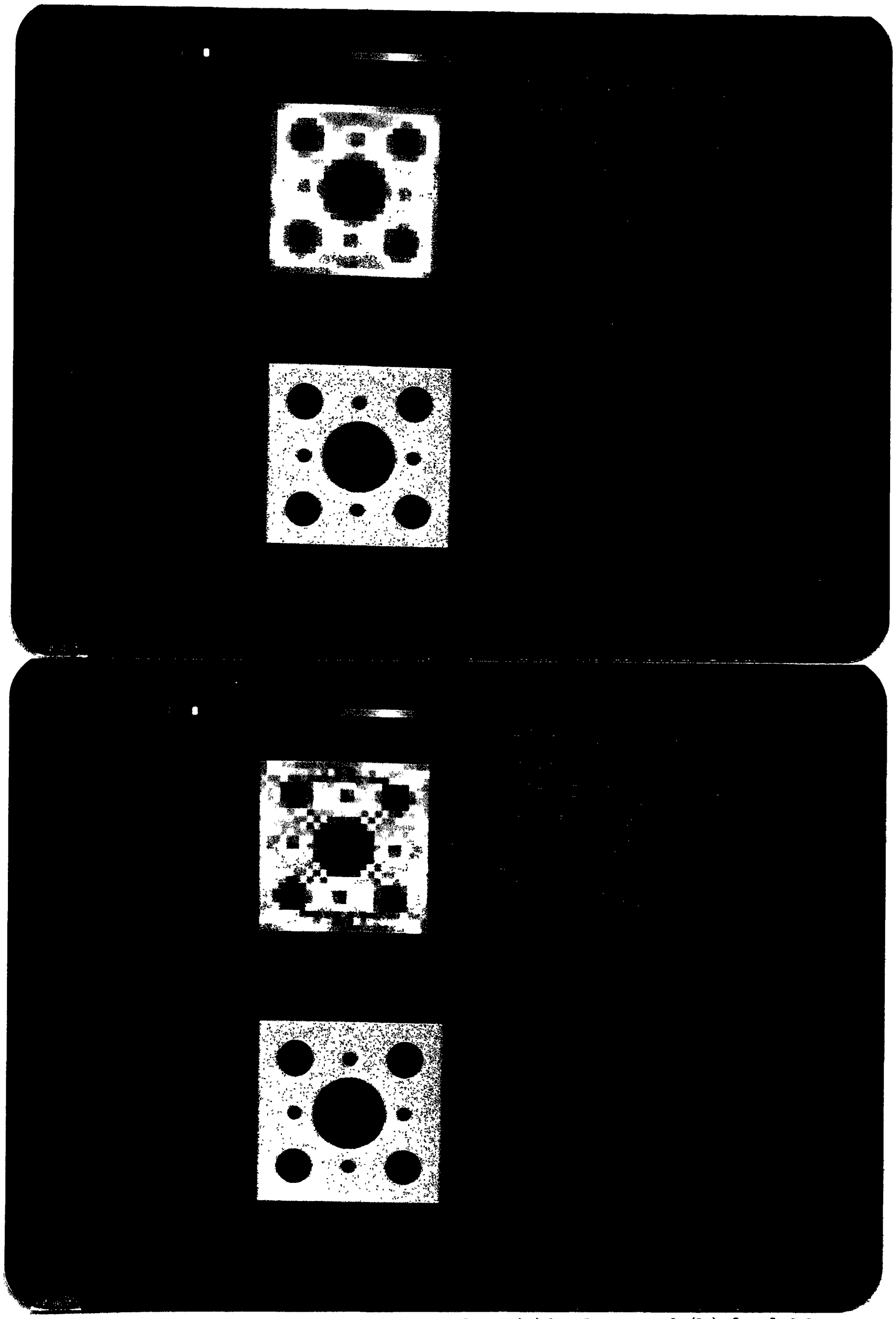

Figure 5.8: Reconstruction of Sample 6 (a)for **h54** and (b) for **h99**

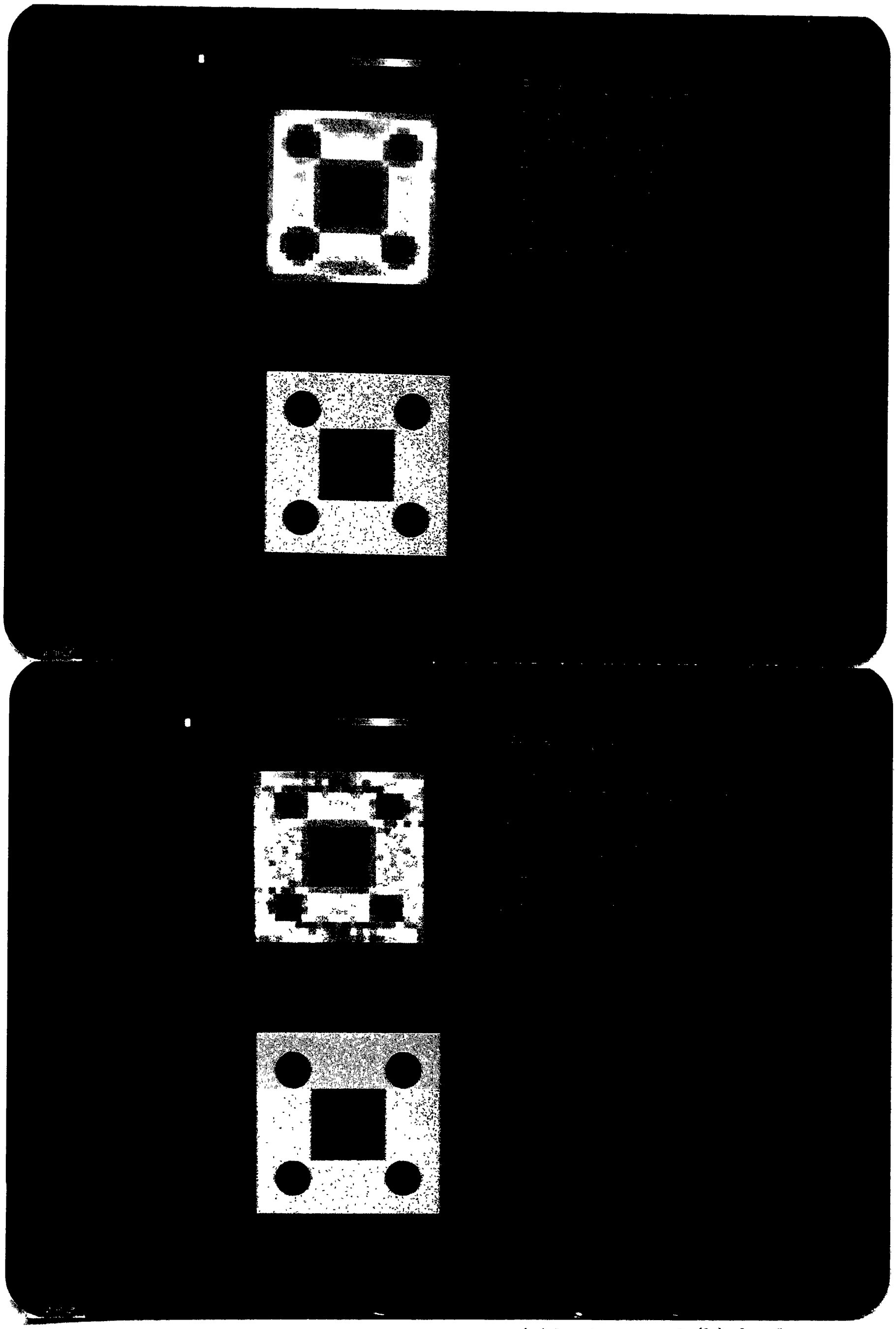

Figure 5.9: Reconstruction of Sample 7 (a)for **h54** and (b) for **h99**

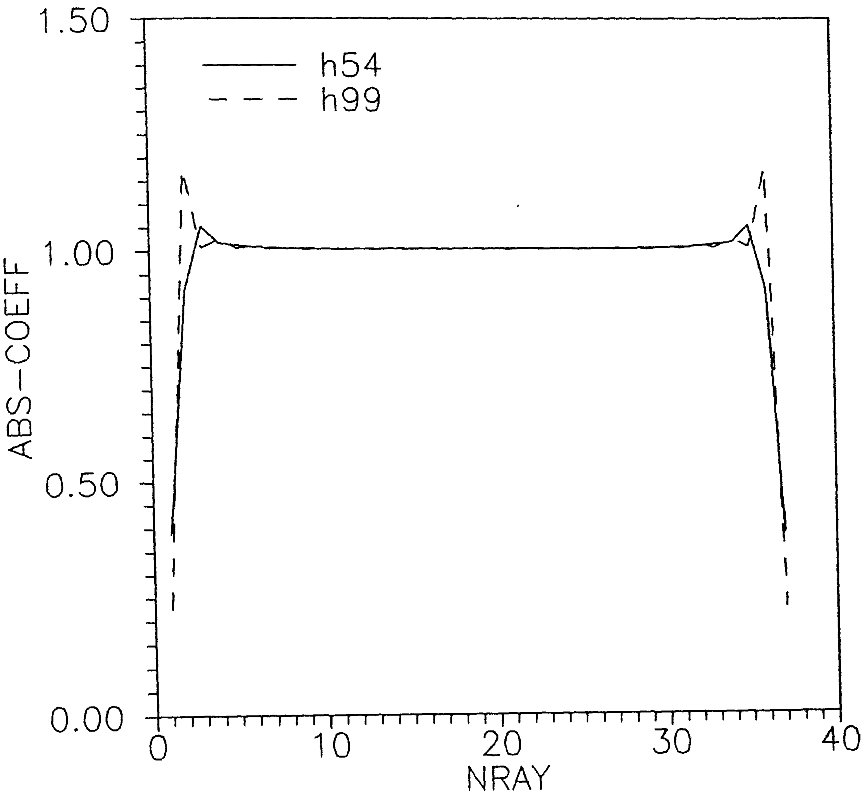

Fig. 5.10: Horizontal Centerline plot of sample 1

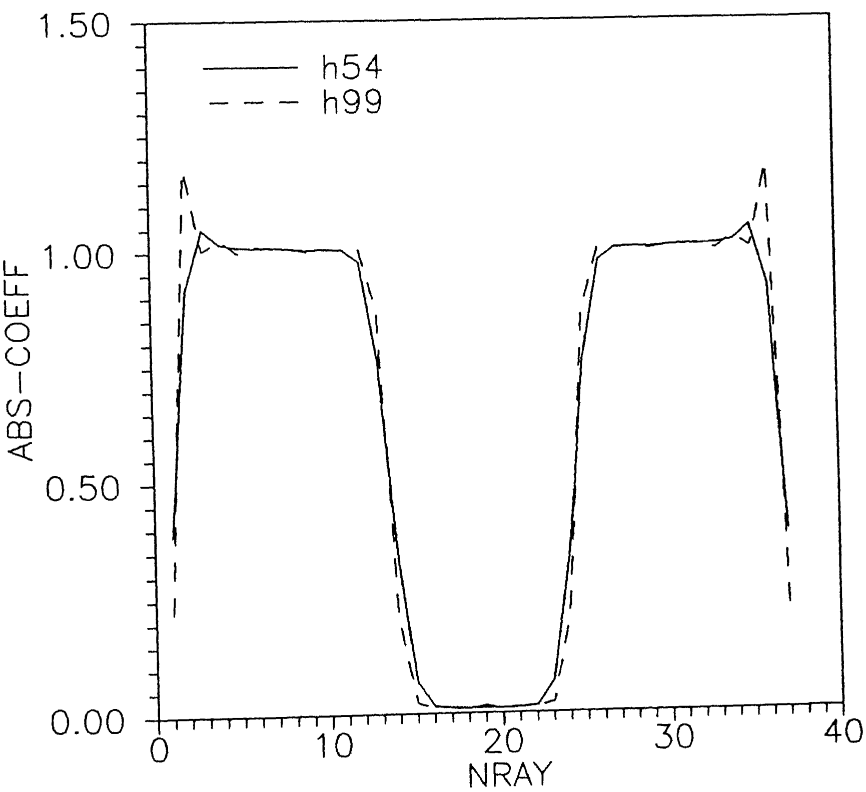

Fig. 5.11: Horizontal Centerline plot of sample 2

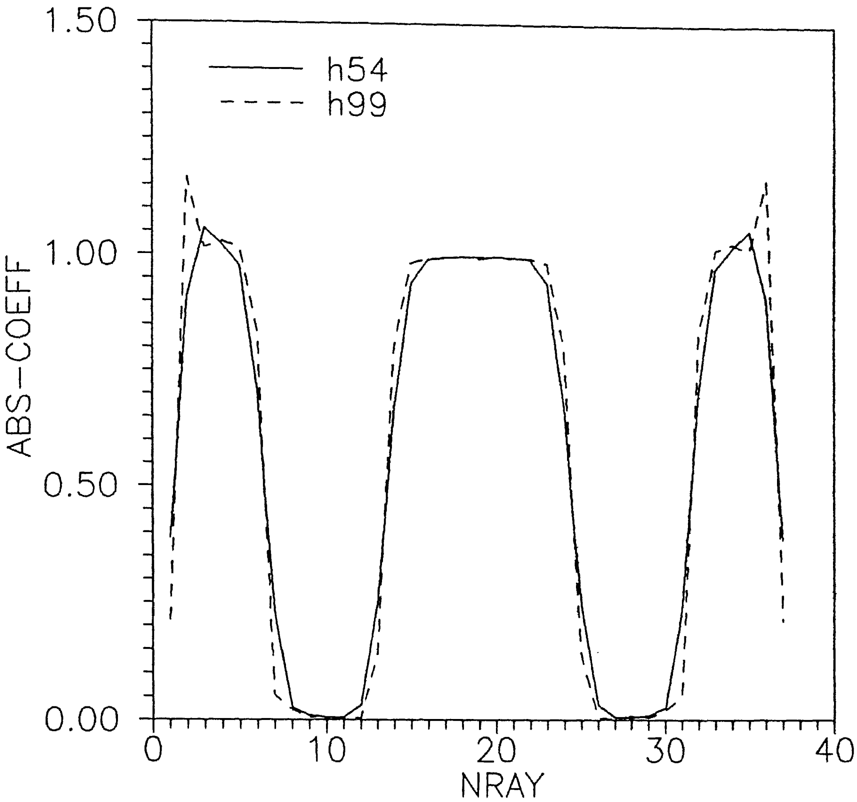

Fig. 5.12: Horizontal Centerline plot of sample 3

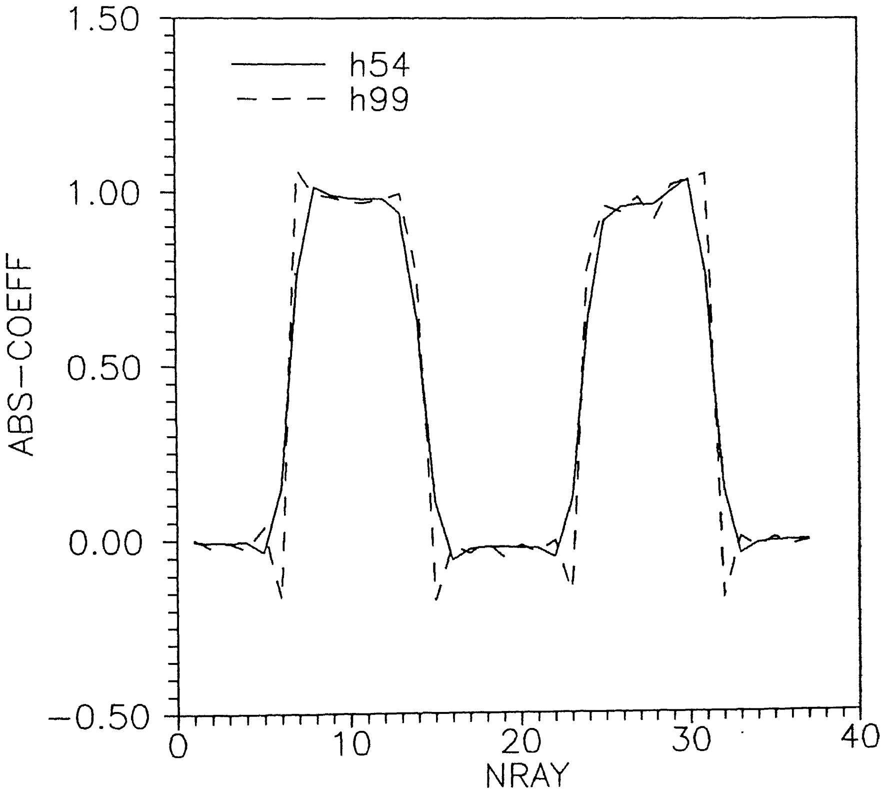

Fig. 5.13: Horizontal Centerline plot of sample 4

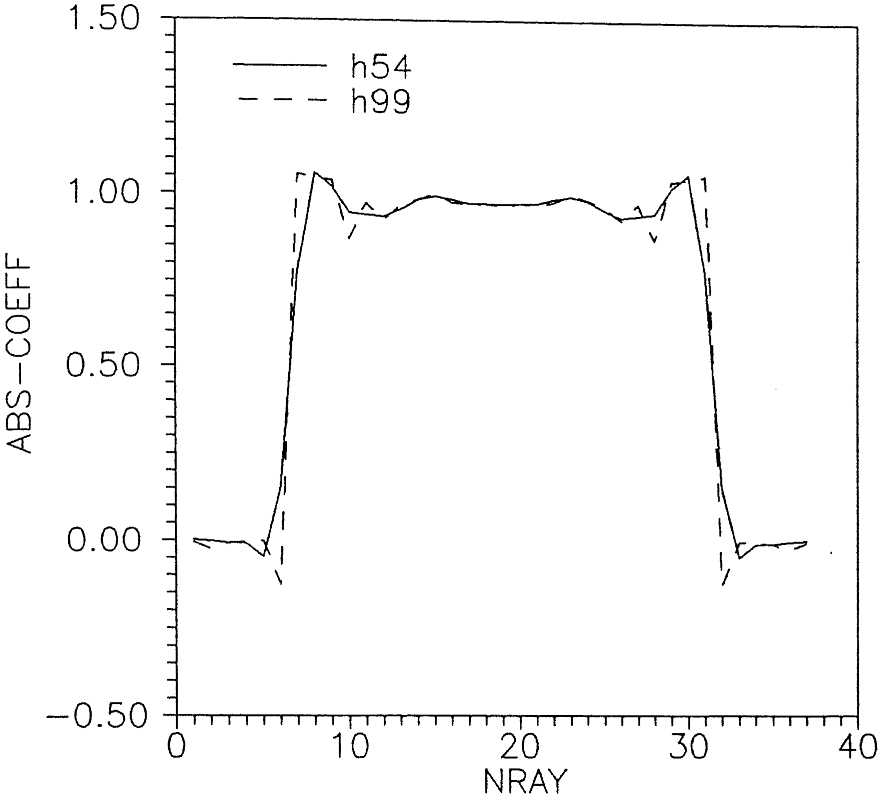

Fig. 5.14: Horizontal Centerline plot of sample 5

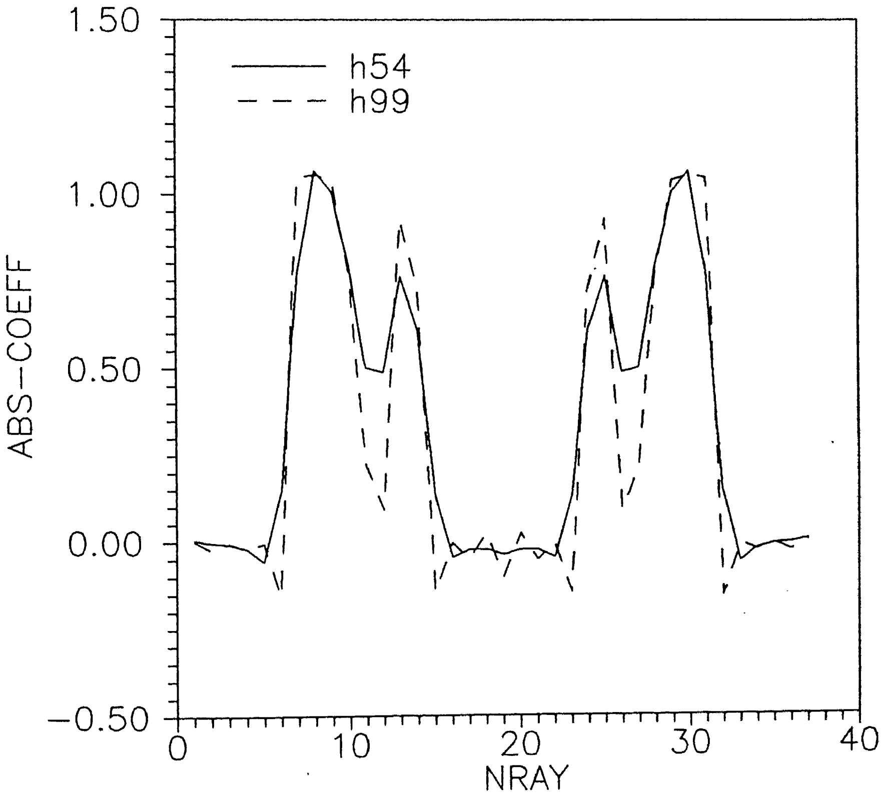

Fig. 5.15: Horizontal Centerline plot of sample 6

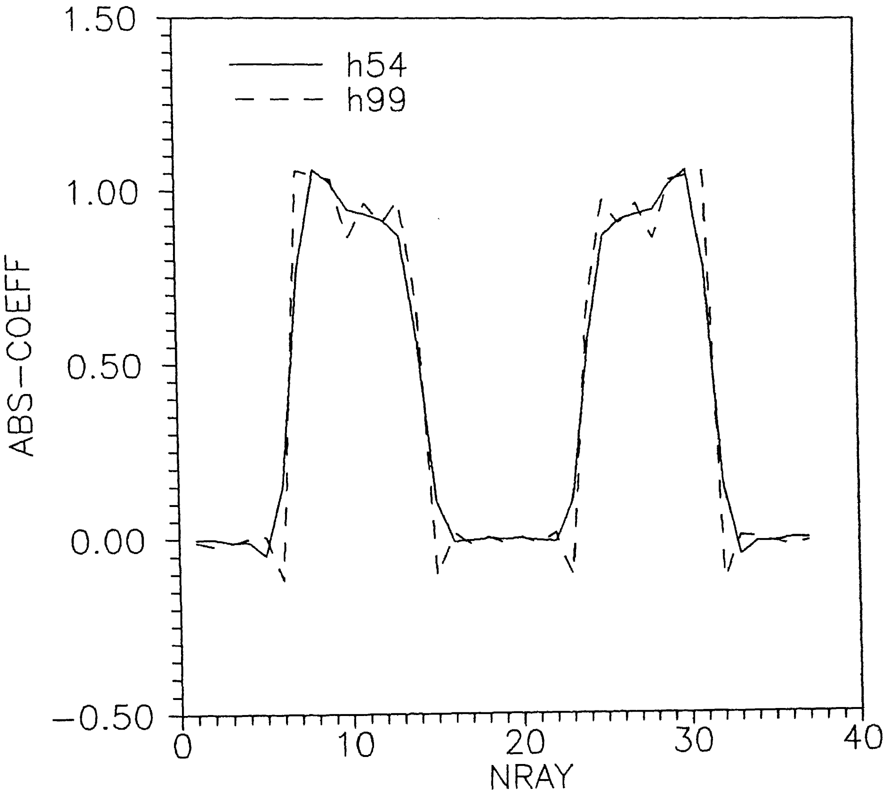

Fig. 5.16: Horizontal Centerline plot of sample 7

Chapter 6

Results

In this chapter, the results obtained from data of two phase liquid metal flow system, have been presented. The objective of the study in this chapter is to:

- visualise the flow.
- compare the reconstructed void-fraction distribution (nitrogen content) using CBP algorithm with those from Chord-Segment-Inversion (CSI) algorithm used by Jayakumar(1996),
- study the effect of filters.
- study the symmetry aspect of two halves of pipe flow.
- study flow variation with height.
- study flow variation with volume flow rate of Nitrogen.

6.1 Colour Visualisation of flow System

The reconstructed images and horizontal centerline plots are shown in Figs. 6.1-6.16. The key to photographs has been explained in chapter 5. The only difference

Sample	Nray	h54	h99	CSI	LSS
BN600	37	0.2297	0.2310	0.2593	0.2593
BS600	37	0.2190	0.2235	0.2426	0.2424
BS400	37	0.1593	0.1611	0.1731	0.1730
TS400	37	0.2212	0.2225	0.2505	0.2507
BN400	19	0.1577	0.1599	0.1868	0.1886
TN400	19	0.2484	0.2479	0.2947	0.2952
TN600	19	0.3125	0.3146	0.3751	0.3757
TS600	19	0.2774	0.2773	0.3355	0.3360

Table 6.1: Comparing the Area Averaged values of void fraction from the CBP and the CSI & LSS algorithms

is that here all the details have been shown on the bottom part of the photographs, and here the colour code bar is shown vertical. The scale (values at two ends and at the center) shows the actual void-fraction corresponding to the colour code.

Let us take Fig. 6.1(a) (corresponding to h54 filter) for illustration, in the center we see green colour which upon interpolation gives a void fraction of roughly 0.34 which can also be seen from Fig. 6.2. In a similar fashion, at any pixel the image gives the approximate value of void fraction and thus helps in visualisation of the two phase flow system, e.g., reconstruction of BN600 for h54 filter (Fig. 6.1(a)) illustrates that the void fraction in the center is more (shown by yellow as compared to indigo at periphery). This means nitrogen tends to get concentrated in the center and mercury remains at the periphery. Other cases can also be similarly interpreted.

6.2 Comparing CBP and CSI results

There are 8 sets of data: first four sets correspond to 2 mm spacing (NRAY=37) and last four to 4 mm spacing (NRAY=19). The area averaged void fraction for filter h54 and h99 have been compared with those of CSI & LSS algorithms (obtained from Jayakumar(1996)) in Table 6.1.

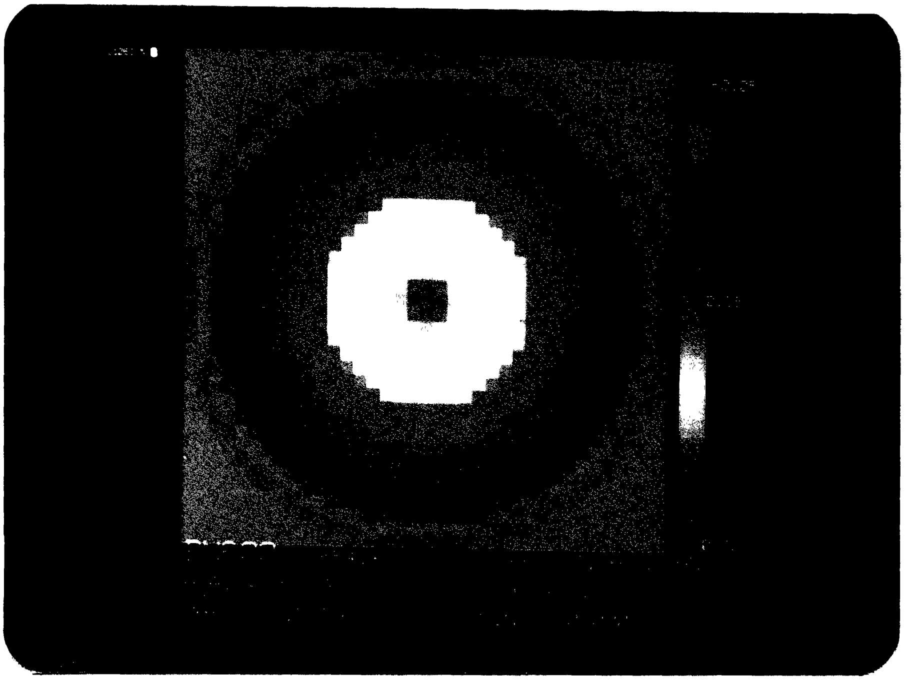

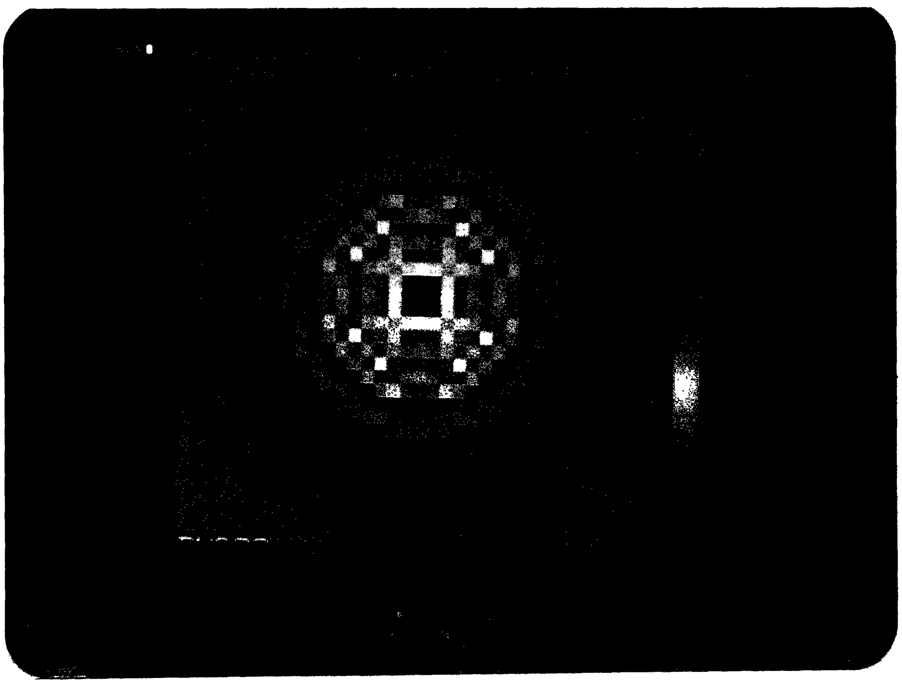

Figure 6.1: Reconstruction of BN600 (a) for **h54** and (b) for **h99**

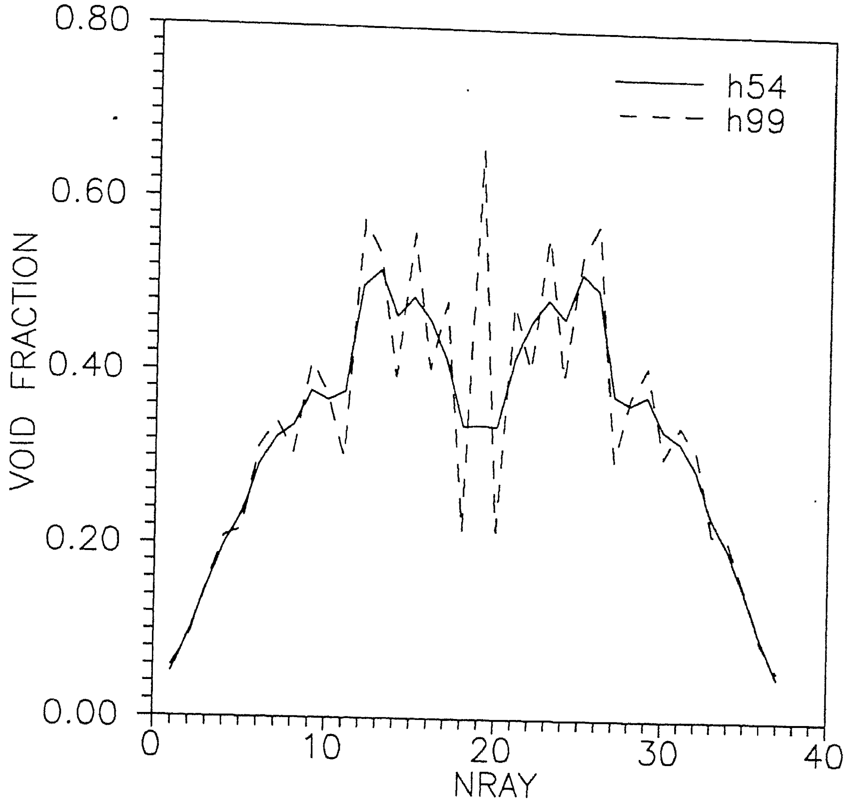

Fig. 6.2 : Horizontal Centerline plot of BN600

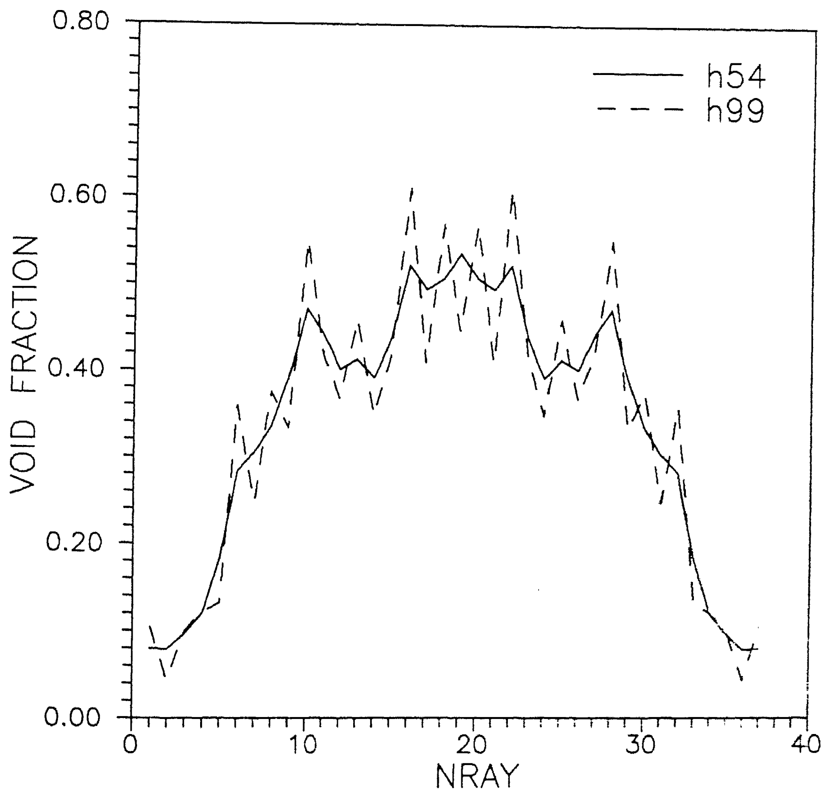

Fig. 6.3 : Horizontal Centerline plot of BS600.

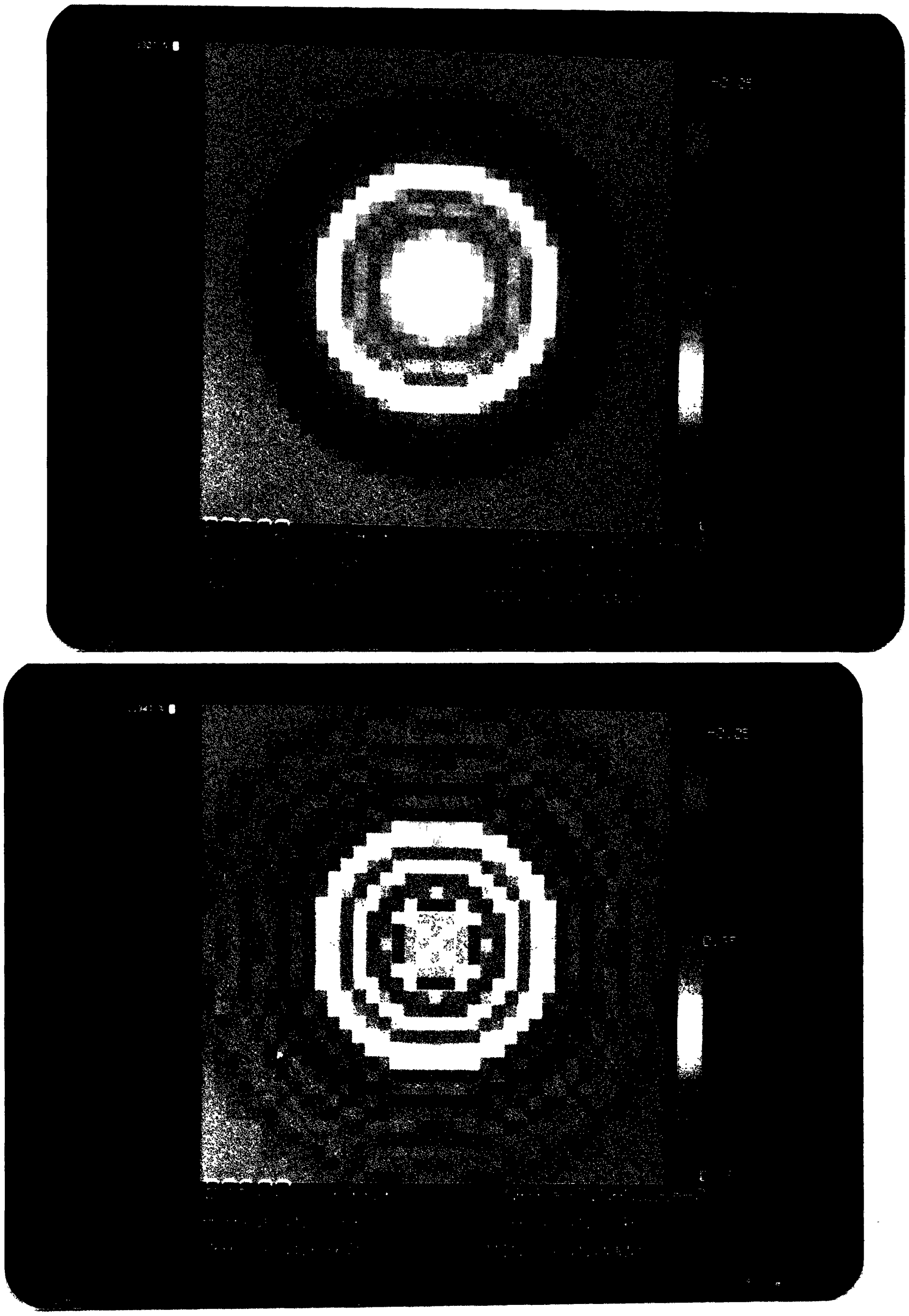

Figure 6.4: Reconstruction of BS600 (a) for **h54** and (b) for **h99**

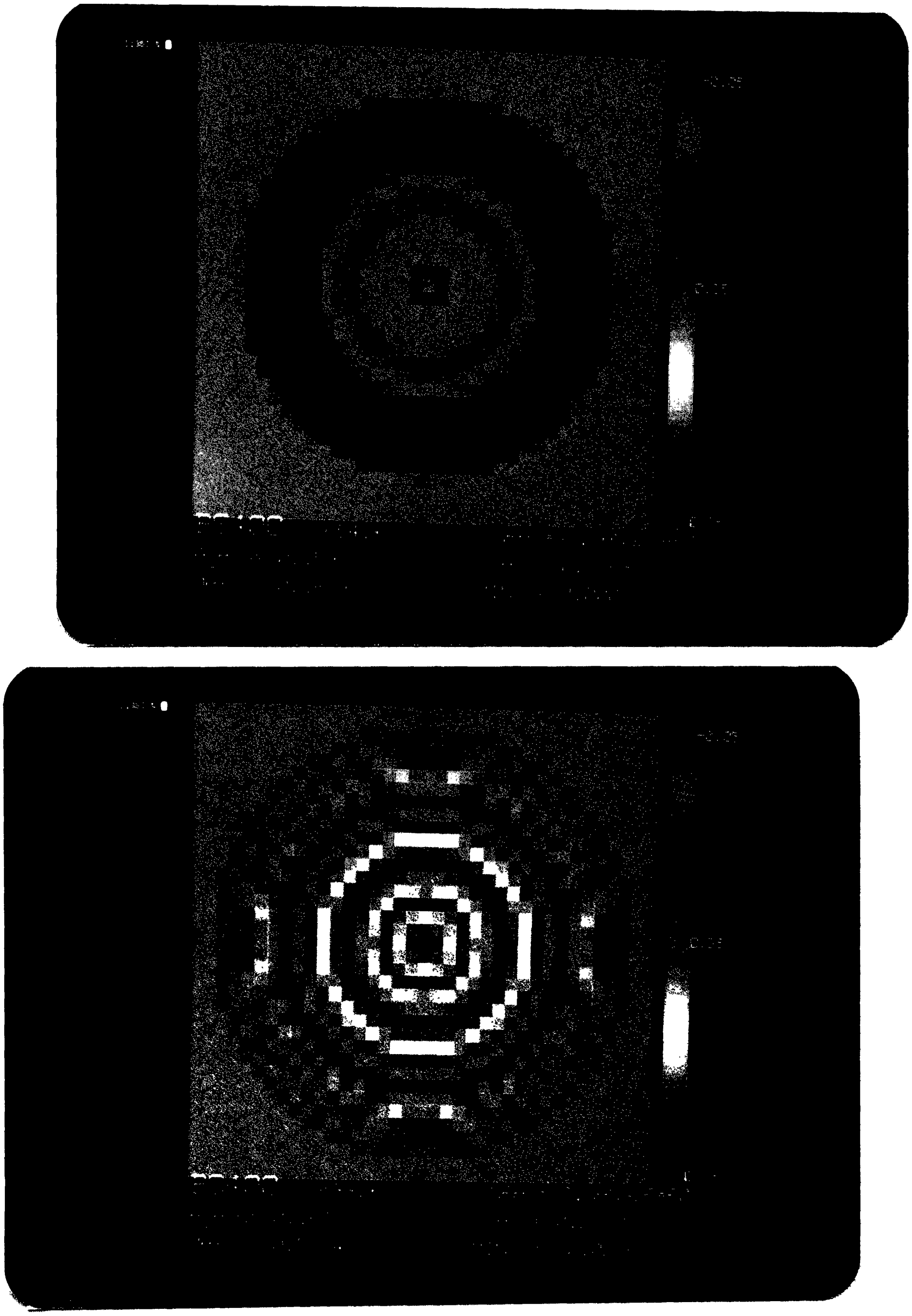

Figure 6.5: Reconstruction of BS400 (a) for **h54** and (b) for **h99**

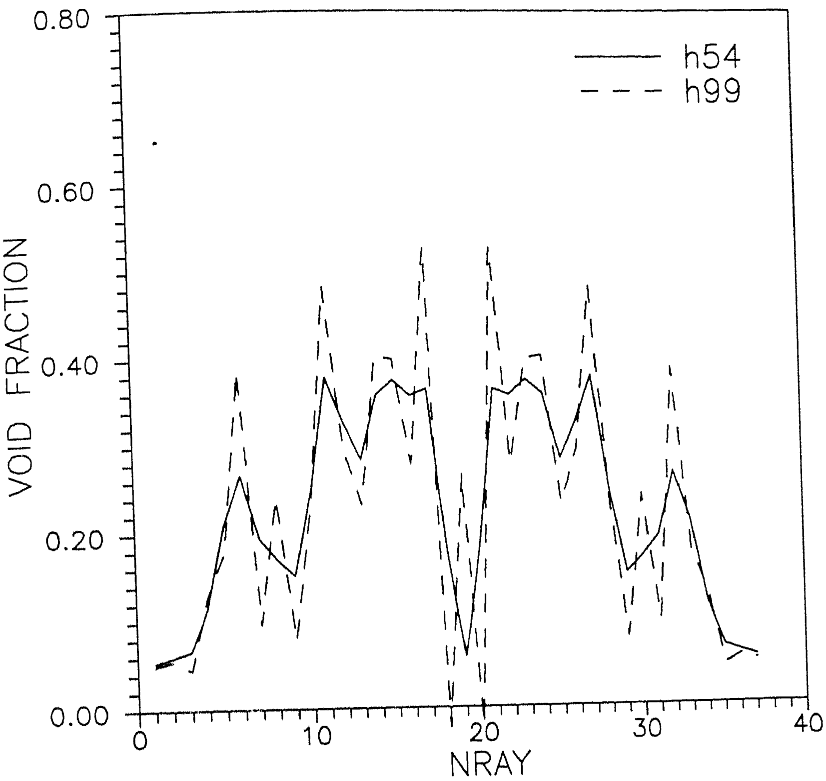

Fig. 6.6 : Horizontal Centerline plot of BS400.

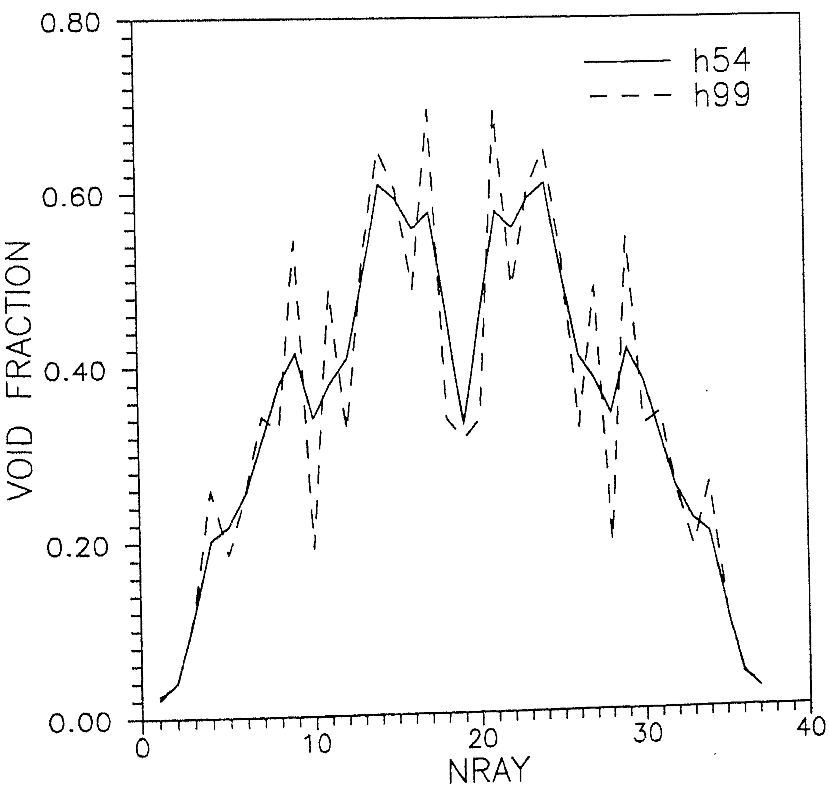

Fig. 6.7 : Horizontal Centerline plot of TS400

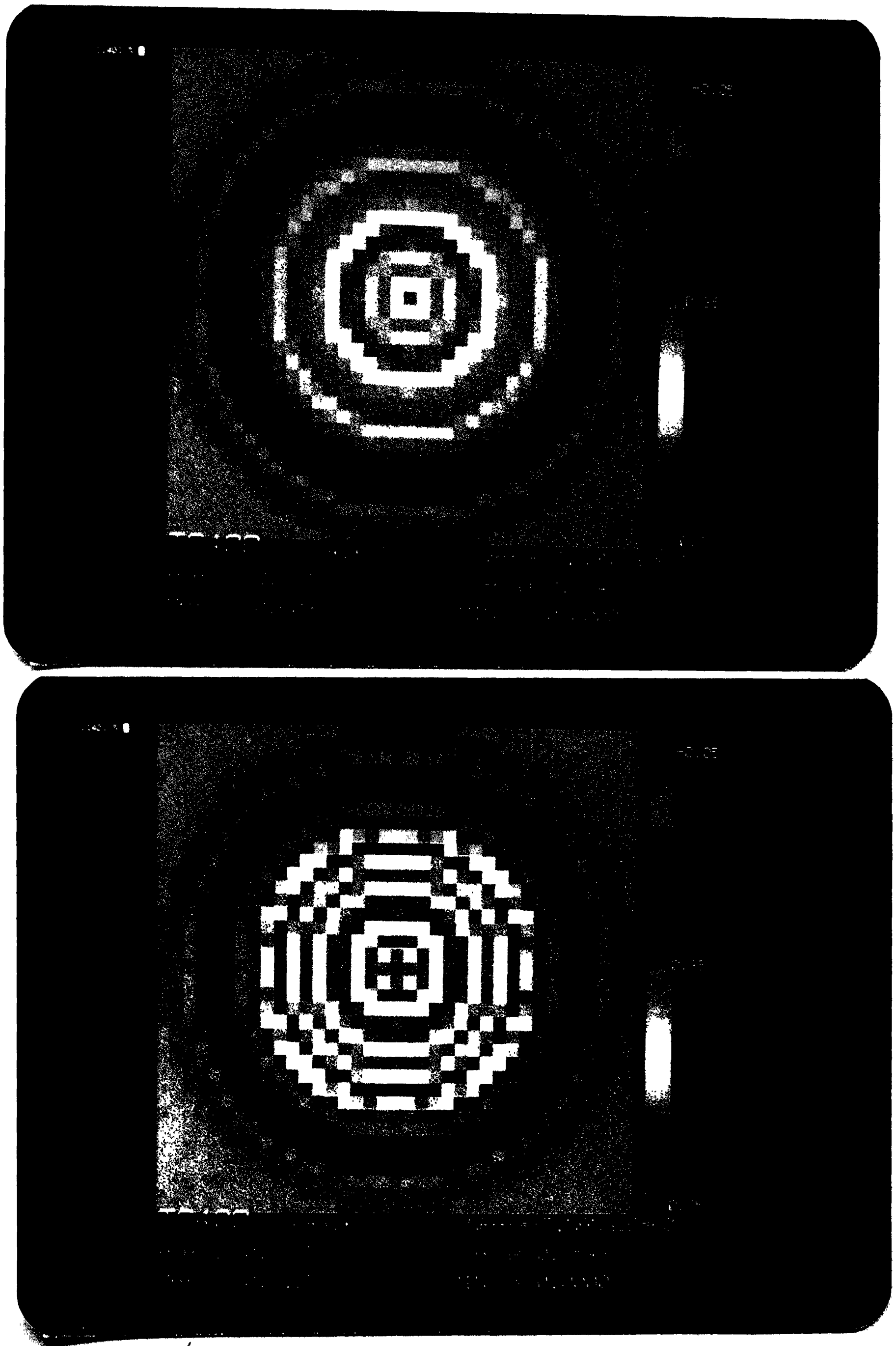

Figure 6.4: Reconstruction of TS400 (a) for **h54** and (b) for **h99**

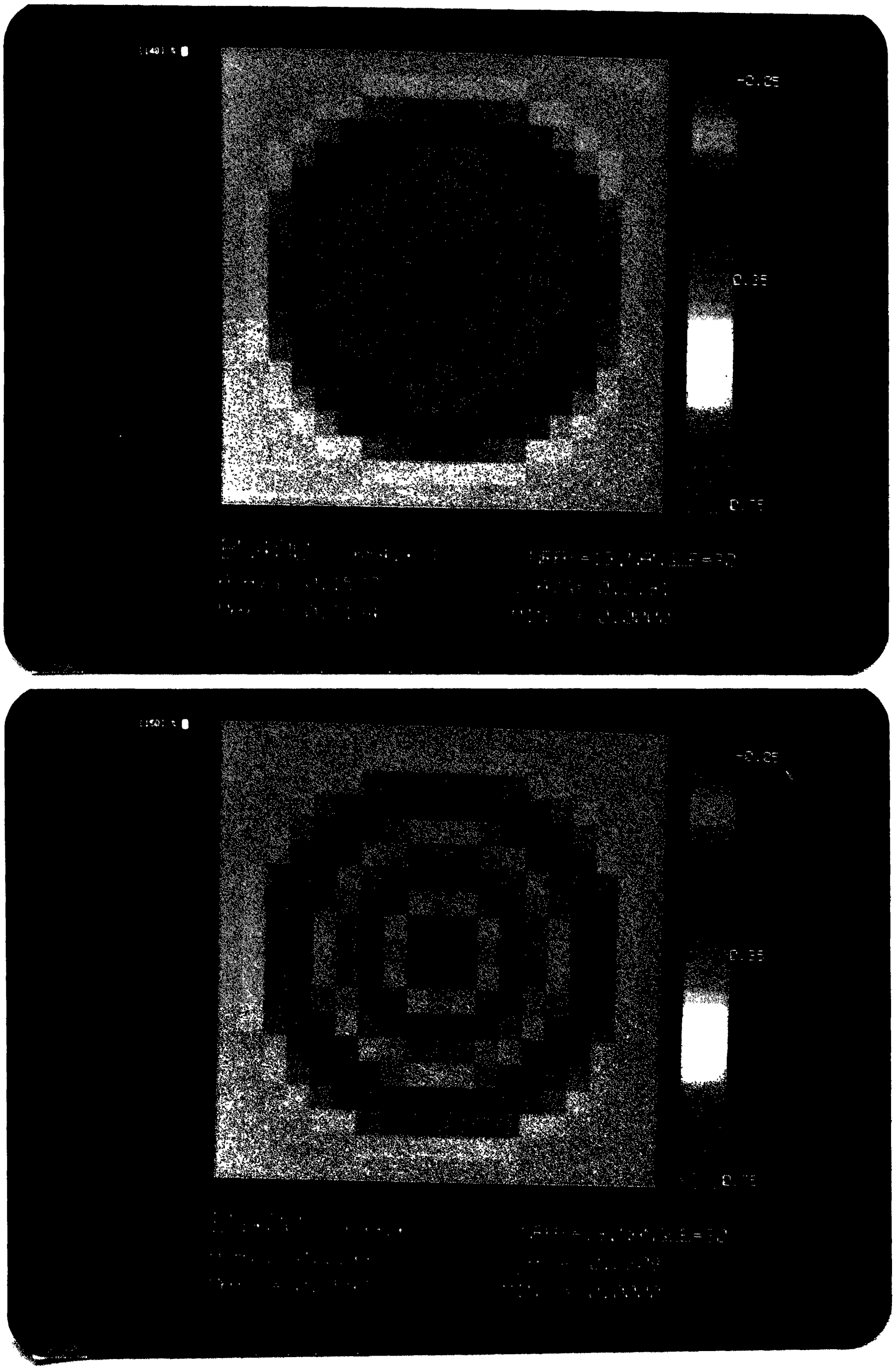

Figure 6.9: Reconstruction of BN400 (a) for **h54** and (b) for **h99**

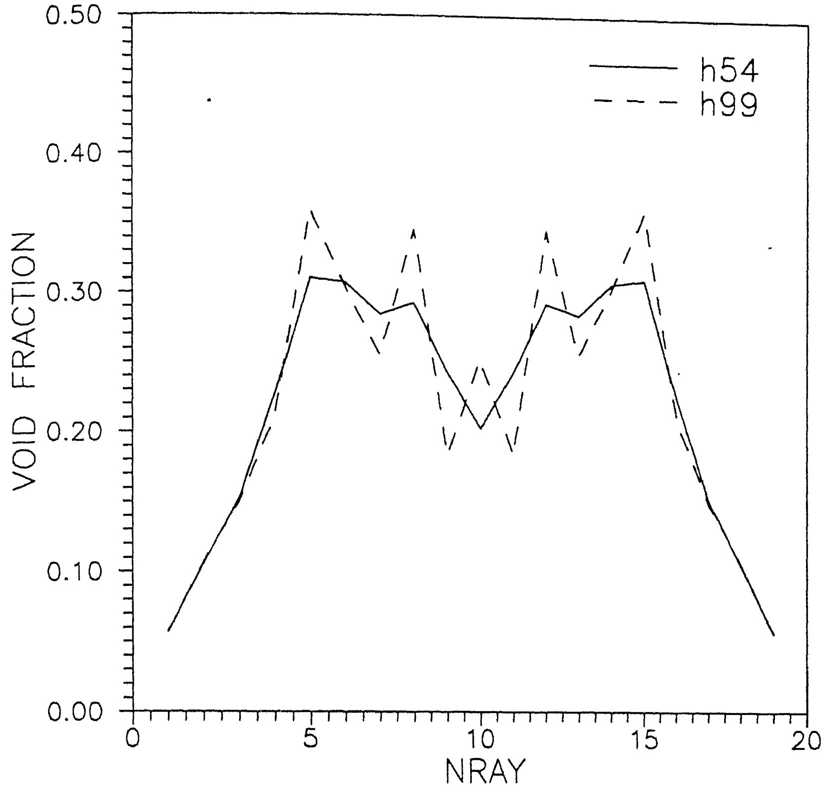

Fig. 6.10: Horizontal Centerline plot of BN400

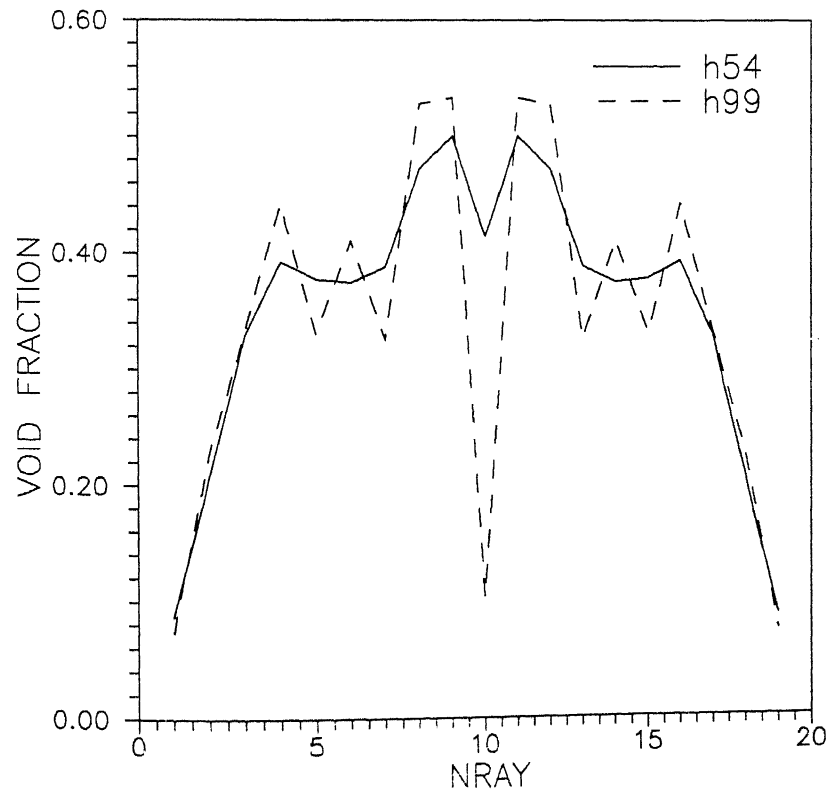

Fig. 6.11: Horizontal Centerline plot of TN400

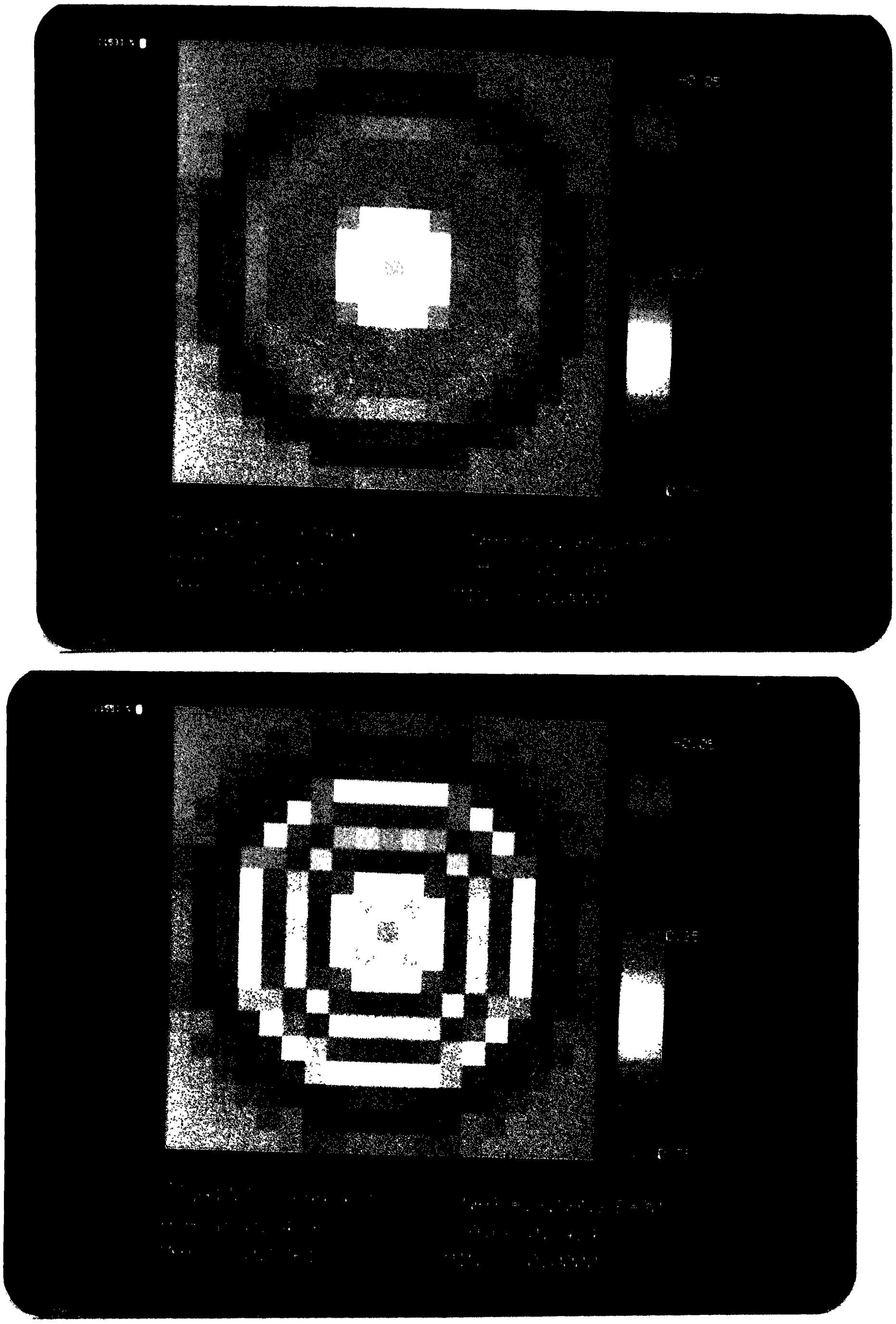

Figure 6.12: Reconstruction of TN400 (a) for **h54** and (b) for **h99**

Figure 6.13: Reconstruction of TN600 (a) for **h54** and (b) for **h99**

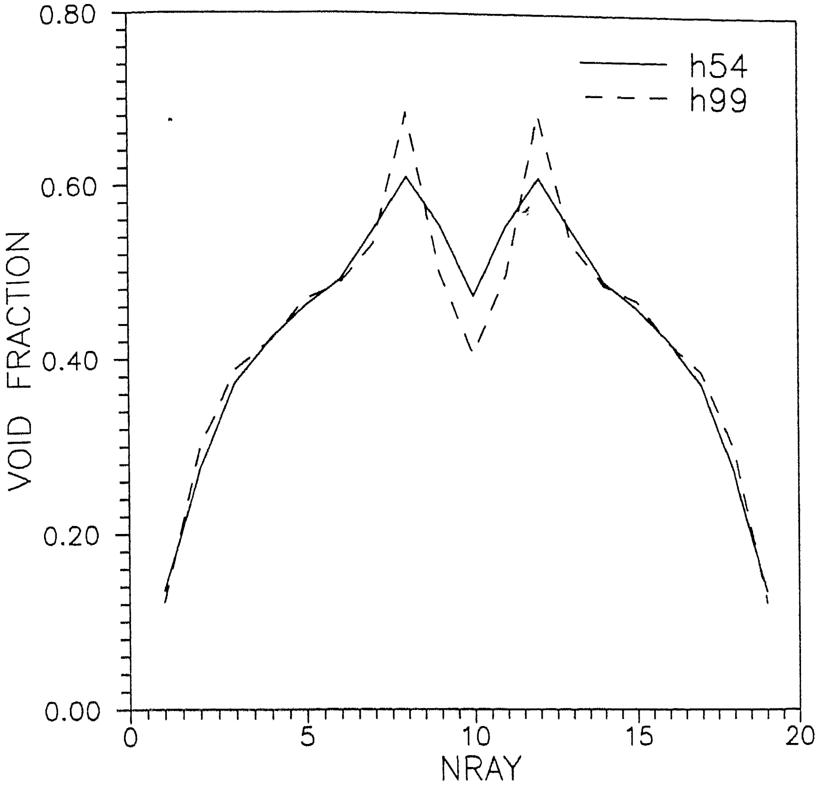

Fig. 6.14: Horizontal Centerline plot of TN600

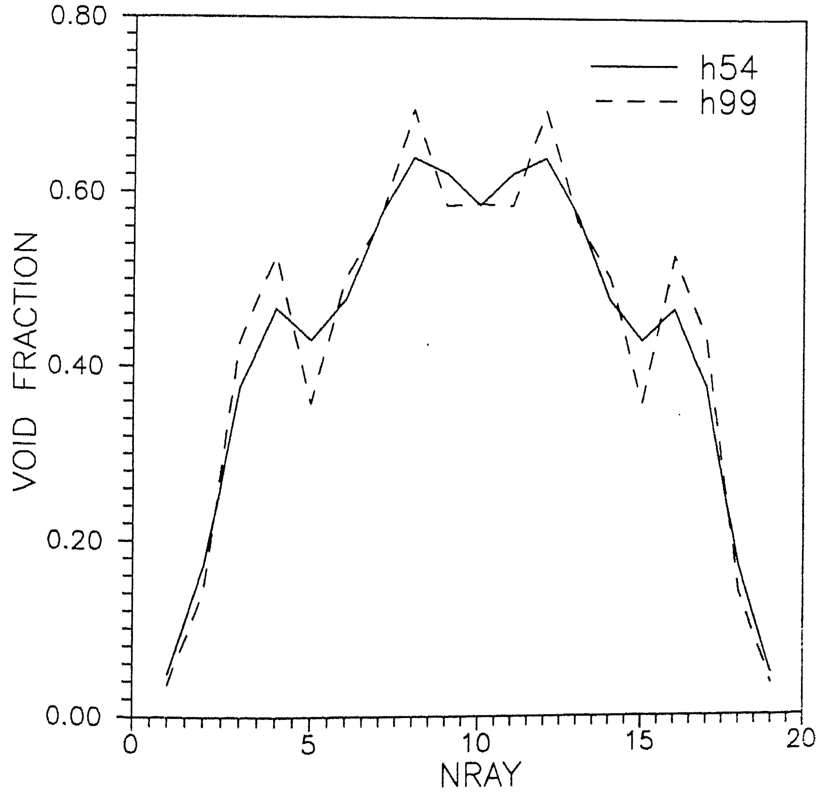

Fig. 6.15: Horizontal Centerline plot of TS600

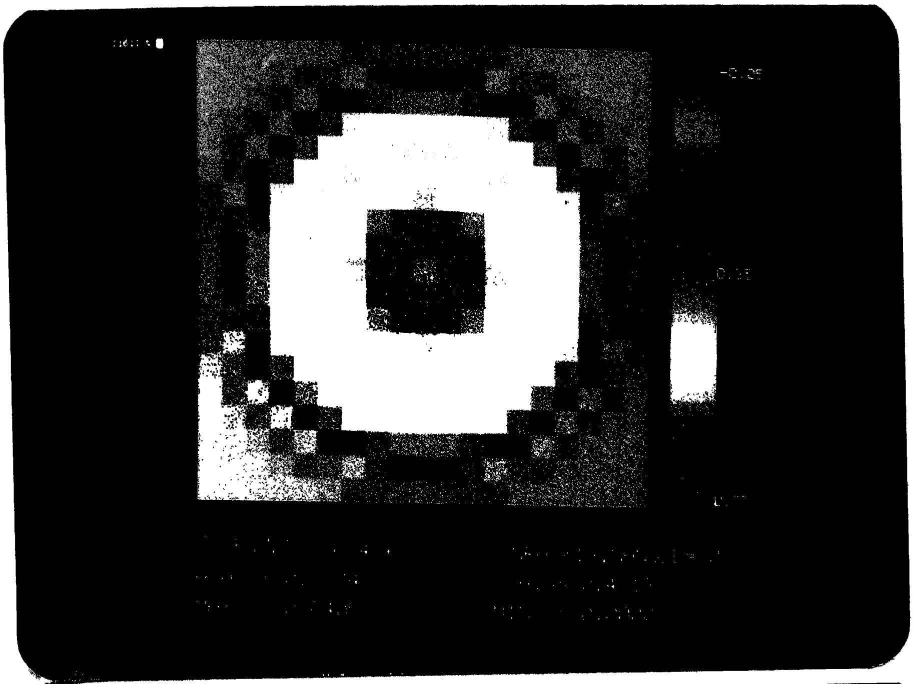

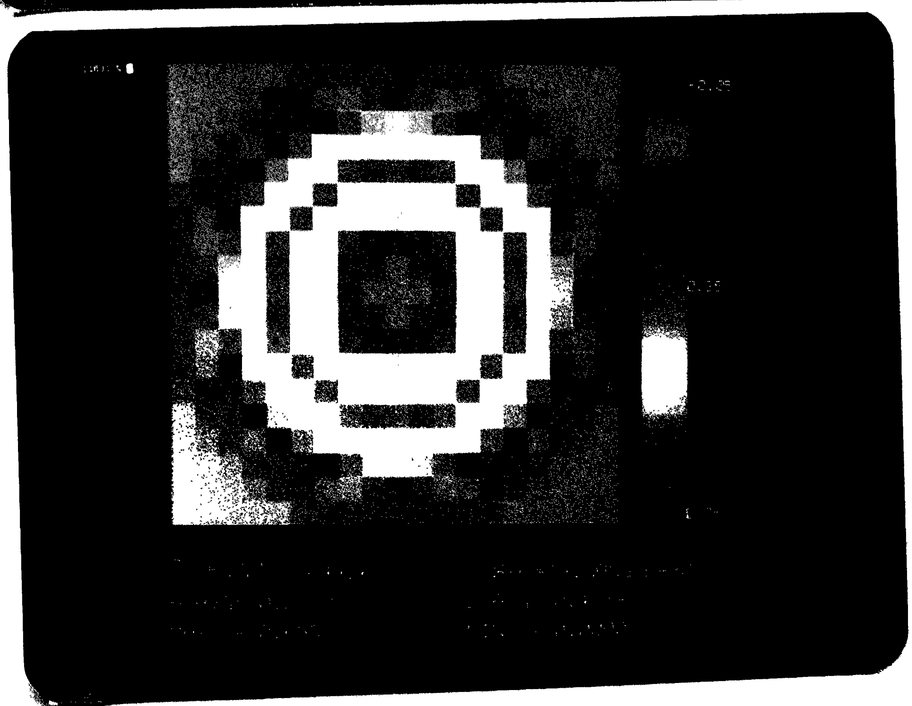

Figure 6.16: Reconstruction of TS600 (a) for **h54** and (b) for **h99**

The results obtained are comparable with those obtained by Jayakumar(1996) for same data sets. Values obtained by CBP are on the lower side as compared to CSI or LSS. Void fraction obtained by h99 are higher as compared to those obtained by h54.

6.3 Effect of Filters

In view of the error theory, the results of two Hamming filters are compared. Details of Hamming filters have been incorporated in section 3.3. The filter h54 is smooth h99 sharp. This is reflected in reconstructed images where variations are smoothened out by h54 comparing Fig. 6.1(a)-(b) and Fig. 6.2, void fraction in the center is very high for h99 (0.66, shown by red dot at center) as compared to h54 (0.34, shown by green patch at the center). Then we see rings of green-yellow and red-yellow for the case of h99 filter as compared to relatively smooth yellow for h54 filter.

The results for all 8 data set have been summarised in Table 6.2.

	NMAX		NMIN		A-AVG		C-AVG	
Sample	h54	h99	h54	h99	h54	h99	h54	h99
BN600	0.5259	0.6602	0.00	0.00	0.2297	0.2310	0.3337	0.3400
BS600	0.5357	0.6260	0.00	0.00	0.2190	0.2239	0.3362	0.3362
BS400	0.3839	0.5724	0.00	-0.023	0.1593	0.1611	0.2269	0.2280
TS400	0.6092	0.7125	0.00	0.00	0.2212	0.2225	0.3543	0.3543
BN400	0.3134	0.3597	0.00	0.00	0.1577	0.1599	0.2191	0.2208
TN400	0.5003	0.57613	0.00	0.00	0.2484	0.2479	0.3509	0.3424
TN600	0.6109	0.6871	0.00	0.00	0.3125	0.3146	0.4329	0.4323
TS600	0.6405	0.6952	0.00	0.00	0.2774	0.2773	0.4318	0.4358

Table 6.2: Summary of results for two-phase flow data for h54 and h99 filters

6.4 Effect of Symmetry

Data used in this study has been collected for two halves separately, and for only one view. One of the basic aim of this study is also to verify whether the flow is radially symmetric. For reconstructing an image using CBP algorithm, line integral data from different views are required. In the present study, for the purpose of reconstructing the images, the flow system was assumed to be radially symmetric. The data being available for two halves independently, the same was replicated and two halves of data were used separately to reconstruct the image.

We have studied two cases for both the filters, h54 and h99.

- Study of TN600 & TS600 (corresponding to 4 mm ray scan spacing)
- Study of BN600 & BS600 (corresponding to 2 mm ray scan spacing)

The lack of circular symmetry is evident by looking at the reconstructed images of two halves, i.e., North half & South half (compare Fig. 6.1 & Fig. 6.4). For a quick comparision horizontal centerline plot of TN600 & TS600 (Fig. 6.17) and that of BN600 & BS600 (Fig. 6.18) for h99 filters are shown. We see a red (high) dot at the center in case of BN600 in case of BN600 for h99 filter (Fig. 6.1(b)) and a yellow (low) dot in case of BS600 for same filter.

Thus it is suggested that the data should be collected for more number of views so that $p(s, \theta)$, given by Eq.(2.3), is representative of the non-symmetric flow condition,

6.5 Effect of Height

To study how the void fraction (and hence the other flow parameters) vary with height, horizontal centerline plot of TN400 & BN400 (Fig. 6.19) and horizontal centerline plot of TS400 & BS400 (Fig. 6.20) are shown. It is clear that the void fraction increases with the height (see also the colour images of Fig. 6.12, 6.9 and

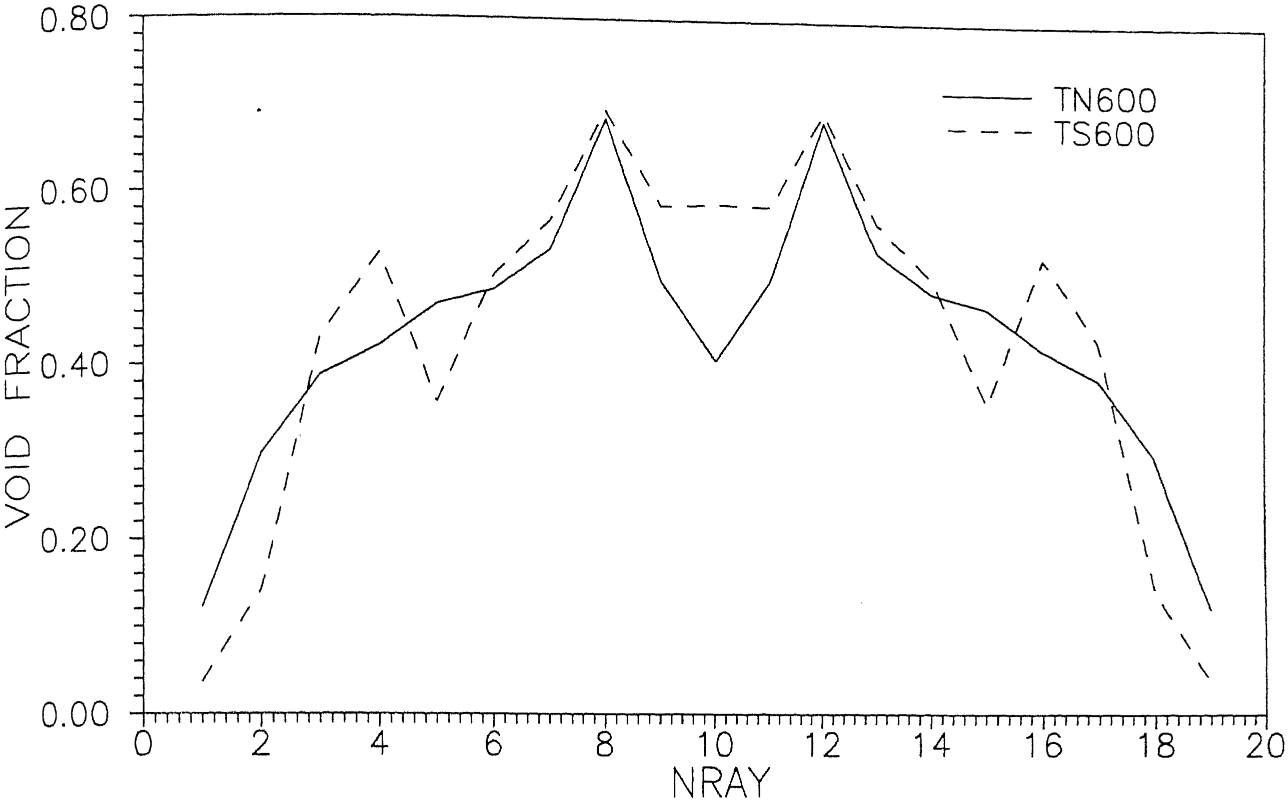

Fig. 6.17: Plot of void fraction of north and south half (TN600 & TS600) for H99 filter

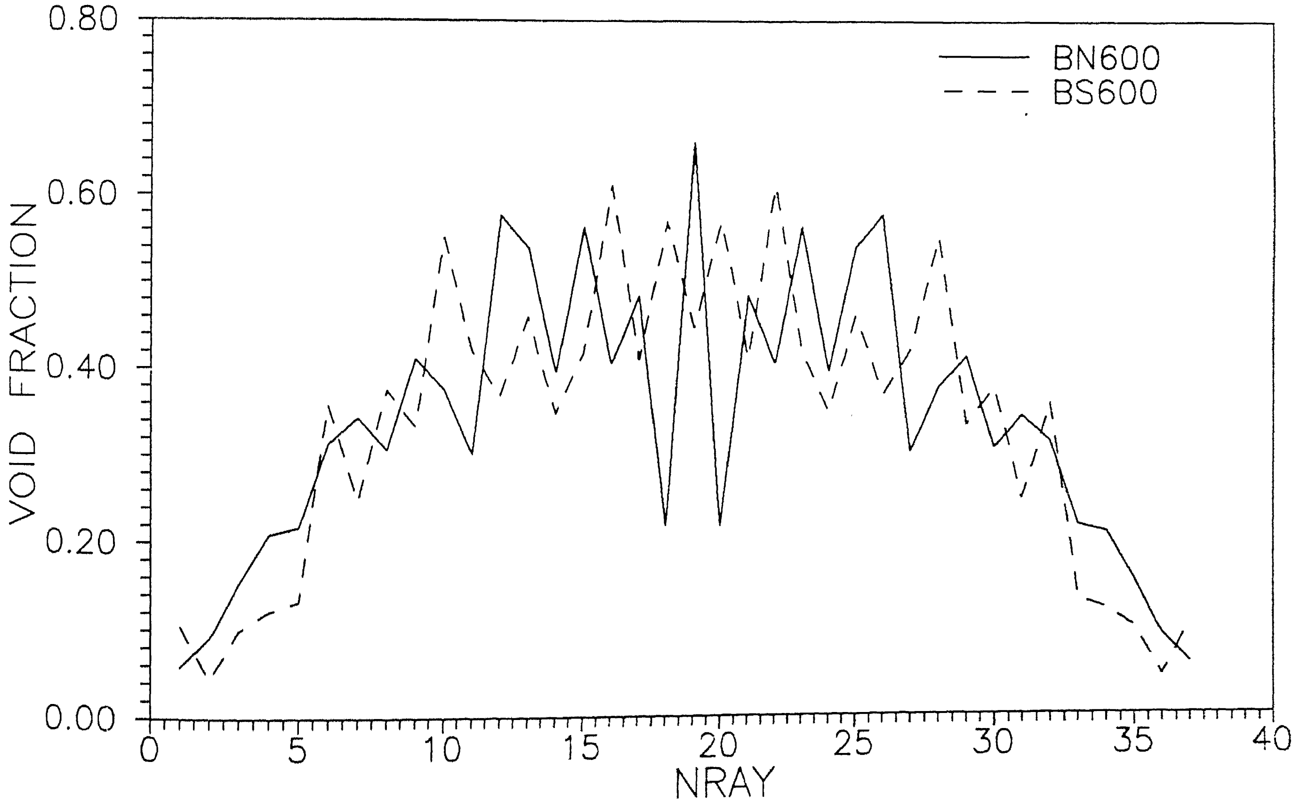

Fig. 6.18: Plot of void fraction of north and south half (BN600 & BS600) for H99 filter

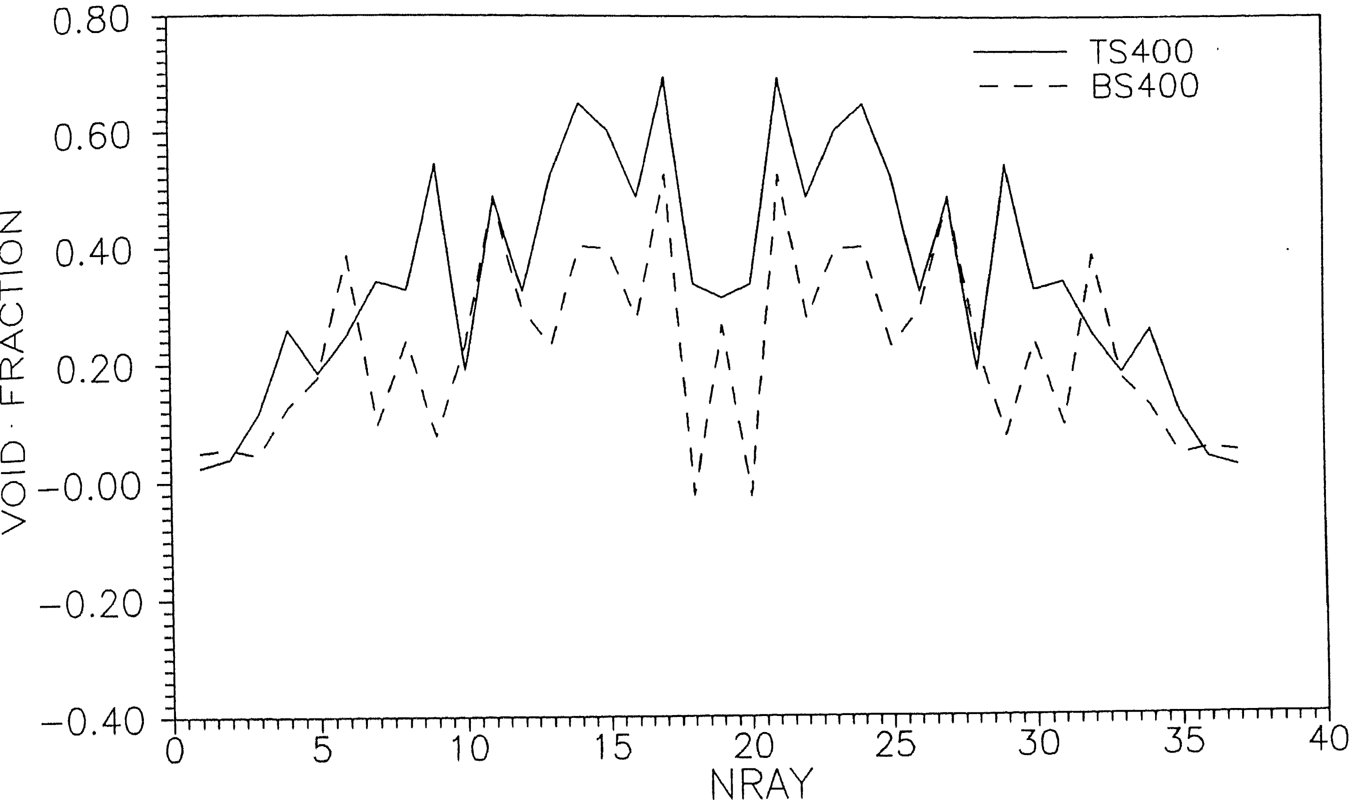

Fig. 6.20: Plot of void fraction of top and bottom (TS400 & BS400) for H99 filter

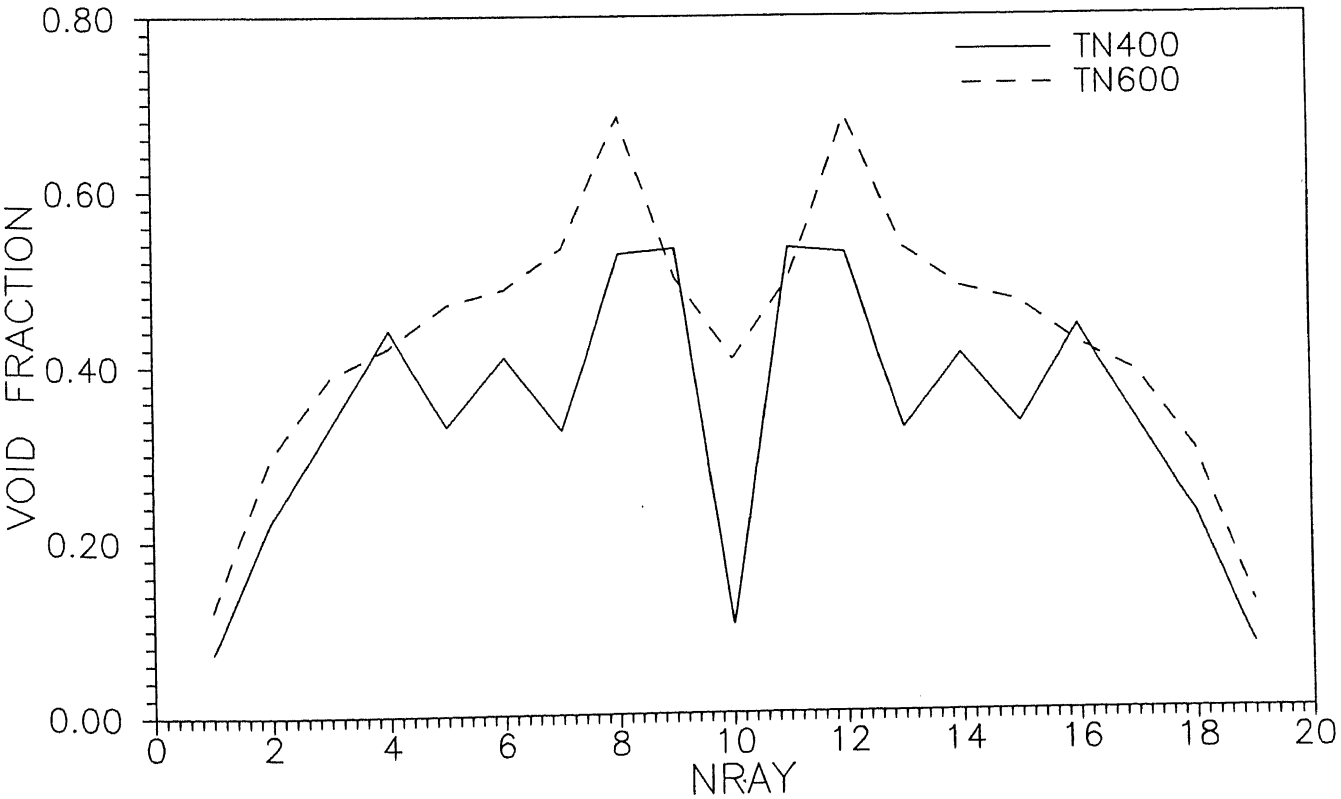

Fig. 6.21: Plot of void fraction of 40 & 60 lpm flow rate (TN400 & TN600) for H99 filter

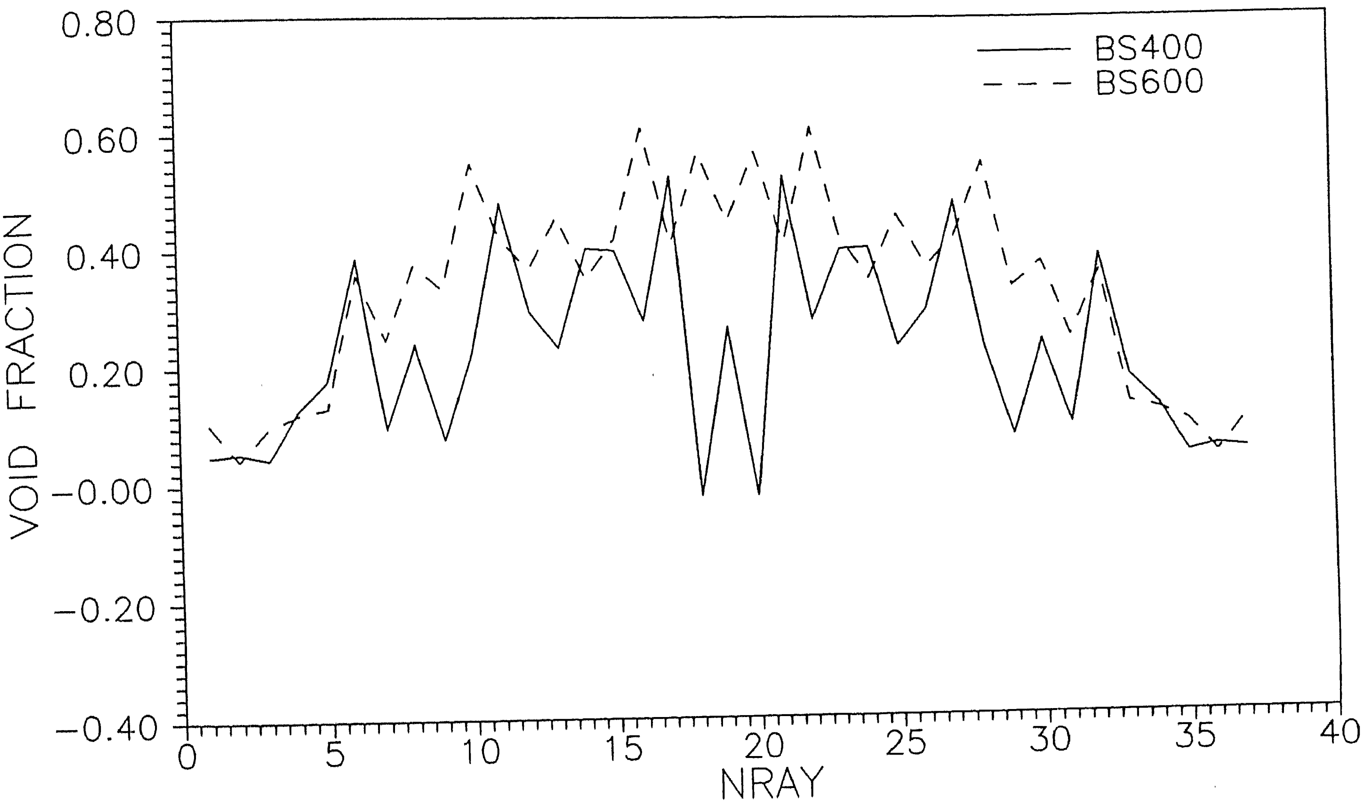

Fig. 6.22: Plot of void fraction of 40 & 60 lpm flow rate (BS400 & BS600) for H99 filter

Chapter 7

Error Analysis

Having reconstructed the image, it is of paramount importance to have some means of measuring the correctness (reliability) of reconstruction. In general, the error consists of two components.

1. error in collecting the data

2. error in reconstruction algorithm

For simulated data the first component of the error is absent and the error is entirely due to the second component. For simulated data, by comparing the actual values and reconstructed values of absorption coefficient, L_2 error (R.M.S. value) has been calculated. For a simulated object it is easier to do show by comparing values pixel-by-pixel the grey level of actual object and reconstructed image. The results have been tabulated in Table 7.1.

But if the object's grey level distribution is unknown, which is generally the case for real data, alternative error representation can be done by $1/NMAX$ (Davis et al.(1995) or relative error (Wells and Munshi(1994)]. The term NMAX has been explained in section 2.3 and relative error has been taken as the R.M.S. value of difference in reconstruction with respect to the Ram-Lak filter. Table 7.2 and Table

Sample	Cos	Sin	H54	H75	H80	H91	H99	Ram
S1	10.20	8.72	10.72	9.33	9.00	8.43	8.12	8.12
S2	10.54	9.00	11.14	9.64	9.27	8.72	8.31	8.31
S3	10.63	8.77	11.40	9.59	9.22	8.49	8.06	8.06
S4	6.32	5.10	6.93	5.66	5.39	4.90	4.80	4.80
S5	6.93	5.83	7.55	6.32	6.08	5.66	5.48	5.48
S6	7.81	6.48	8.49	7.07	6.78	6.32	6.08	6.08
S7	7.81	6.63	8.48	7.21	7.00	6.56	6.32	6.32

Table 7.1: Percentage L_2 Errors for eight different filters

Sample	H54	H75	H80	H91	H99
S1	0.950	0.945	0.940	0.884	0.848
S2	0.950	0.944	0.937	0.881	0.845
S3	0.947	0.941	0.934	0.876	0.840
S4	0.965	0.964	0.961	0.947	0.930
S5	0.943	0.939	0.937	0.922	0.912
S6	0.938	0.933	0.926	0.912	0.901
S7	0.942	0.939	0.934	0.918	0.899
Dir-Del	0.200	0.109	0.098	0.080	0.071

Table 7.2: $1/NMAX$ of simulated data for hamming filters

7.3 show $1/NMAX$ for simulated objects and two-phase flow respectively. While Table 7.4-7.5 show the relative Error with respect to Ram-lak filter for simulated and two-phase flow system respectively.

Refering to section 2.3, for a given cross-sectional distribution $f(r, \phi)$, the point-wise error in reconstruction is proportional to the magnitude of $W''(0)$, provided that the collected data are "perfect", and the specimen character around the point in question is such that Eq.(2.13) is valid [Davis et al.(1995)]. So processing of a given data set by several filters results in a linear relationship between $W''(0)$ and E_1. The plots have been given in from Figs. 7.1-7.12. Fig. 7.3 shows wide variation from linearity for S1, S2 and S3. Since these samples are smooth, $\nabla^2 f$ vanishes

Sample	H54	H75	H80	H91	H99
BN600	1.90	1.81	1.79	1.66	1.51
BS600	1.87	1.76	1.73	1.65	1.60
BS400	2.60	2.13	2.04	1.86	1.75
TS400	1.64	1.55	1.52	1.45	1.40
BN400	3.19	3.00	2.96	2.85	2.78
TN400	2.00	1.87	1.84	1.78	1.74
TN600	1.64	1.55	1.53	1.49	1.46
TS600	1.56	1.50	1.49	1.46	1.44

Table 7.3: $1/NMAX$ of mercury-nitrogen flow data for hamming filters

Sample	H54	H75	H80	H91	H99	Cos	Sin
S1	4.89	2.45	2.00	0.00	0.00	4.00	1.41
S2	5.10	2.65	2.00	0.00	0.00	4.12	1.41
S3	5.74	3.00	2.45	1.00	0.00	4.69	1.41
S4	4.58	2.45	2.00	0.00	0.00	3.61	1.00
S5	4.58	2.45	2.00	0.00	0.00	3.61	1.00
S6	5.29	2.83	2.24	1.00	0.00	4.24	1.41
S7	4.90	2.65	2.00	0.00	0.00	3.87	1.41
Dir-Del	2.45	1.73	1.73	1.73	0.00	1.41	1.73

Table 7.4: Percentage Relative Errors of simulated data w.r.t. Ram-Lak filter

Sample	H54	H75	H80	H91	H99	Cos	Sin
BN600	4.12	2.24	1.73	0.00	0.00	3.46	1.00
BS600	5.29	2.83	2.24	1.00	0.00	4.58	1.41
BS400	6.86	3.74	3.00	1.00	0.00	5.92	2.00
TS400	6.86	3.74	3.00	1.00	0.00	5.92	2.00
BN400	2.65	1.41	1.00	0.00	0.00	2.24	0.00
TN400	4.47	2.45	2.00	0.00	0.00	3.87	1.00
TN600	4.47	2.45	2.00	0.00	0.00	3.87	1.00
TS600	4.90	2.65	2.00	0.00	0.00	3.74	1.00

Table 7.5: Percentage Relative Errors of mercury-nitrogen data w.r.t. Ram-Lak filter

for the major portion of the region and, hence, Eq.(2.13) no longer represents total error in this case. Figs. 7.4-7.7 show good linear fit because for these samples $\nabla^2 f$ exists. Plots of relative error (Fig. 7.9-7.12) also show good linear fit. Thus we have substantiated the alternative measurement of error in case of real data where the actual distribution $f(r.\phi)$ is not known, i.e., it is not possible to compute L_2 error. Some specimen show a random departure from linearity (e.g., S6, Fig. 7.4), while other show nearly parabolic pattern. The apparent parabolic departures from linearity arise from a systemic shift in position of the "maximum" as has been observed by Davis et al.(1996).

We note, however, that the predictions of Eq.(2.13) are reasonably stable. Since linear fit is generally obtained for all three measurement of error, and for both simulated as well as real data sets.

An interesting feature of this filter sensitivity analysis is the uniqueness of each image per the error graph. All graphs are linear, but with a different slopes. Eq.(2.13) predicts that the slope will vary depending upon $\nabla^2 f$, the "smoothness" of the cross-section. Table 7.6 shows the slope, intercept and standard deviation for simulated data sets and different error representation. Table 7.7 shows these details for two phase flow data and the Dirac-delta functional.

Samples	L_2 error			$1/NMAX$			Relerror		
	Slope	Int.	Var. $\times 10^{-4}$	Slope	Int.	Var. $\times 10^{-4}$	Slope	Int.	Var. $\times 10^{-4}$
S1	5.724	7.98	1.58	0.223	0.86	4.51	11.471	-0.37	41.5
S2	6.168	8.19	1.68	0.230	0.86	4.40	11.916	-0.41	38.6
S3	7.313	7.89	2.51	0.236	0.86	4.65	12.482	-0.04	0.528
S4	4.778	4.58	9.50	0.073	0.93	0.524	10.732	-0.32	43.9
S5	4.568	5.31	5.69	0.068	0.91	0.270	10.732	-0.32	43.9
S6	5.294	5.89	5.97	0.082	0.90	0.259	11.456	-0.00	0.471
S7	4.723	6.17	3.65	0.090	0.90	0.628	11.492	-0.37	41.3

Table 7.6: Parameters showing nature of straight line fit of error graph for simulated data

Note : Int. = Intercept, Var. = Variance.

Samples	$1/NMAX$			Relative error		
	Slope	Intercept	Variance	Slope	Intercept	Variance
BN600	0.812	1.573	5.96 $\times 10^{-04}$	9.668	-0.304	4.26 $\times 10^{-03}$
BS600	0.592	1.604	1.10 $\times 10^{-05}$	11.456	-0.006	4.71 $\times 10^{-05}$
BS400	1.857	1.707	1.89 $\times 10^{-04}$	15.165	-0.095	1.67 $\times 10^{-04}$
TS400	0.525	1.408	2.45 $\times 10^{-05}$	15.165	-0.095	1.67 $\times 10^{-04}$
BN400	0.895	2.778	3.65 $\times 10^{-07}$	6.205	-0.222	3.98 $\times 10^{-03}$
TN400	0.568	1.733	7.13 $\times 10^{-06}$	10.499	-0.303	4.70 $\times 10^{-03}$
TN600	0.391	1.456	4.75 $\times 10^{-06}$	10.499	-0.303	4.70 $\times 10^{-03}$
TS600	0.261	1.438	1.43 $\times 10^{-06}$	11.492	-0.375	4.13 $\times 10^{-03}$
Dir-del	0.281	0.056	4.67 $\times 10^{-03}$	4.298	0.674	3.43 $\times 10^{-02}$

Table 7.7: Parameters showing nature of straight line fit of error graph for two-phase flow data

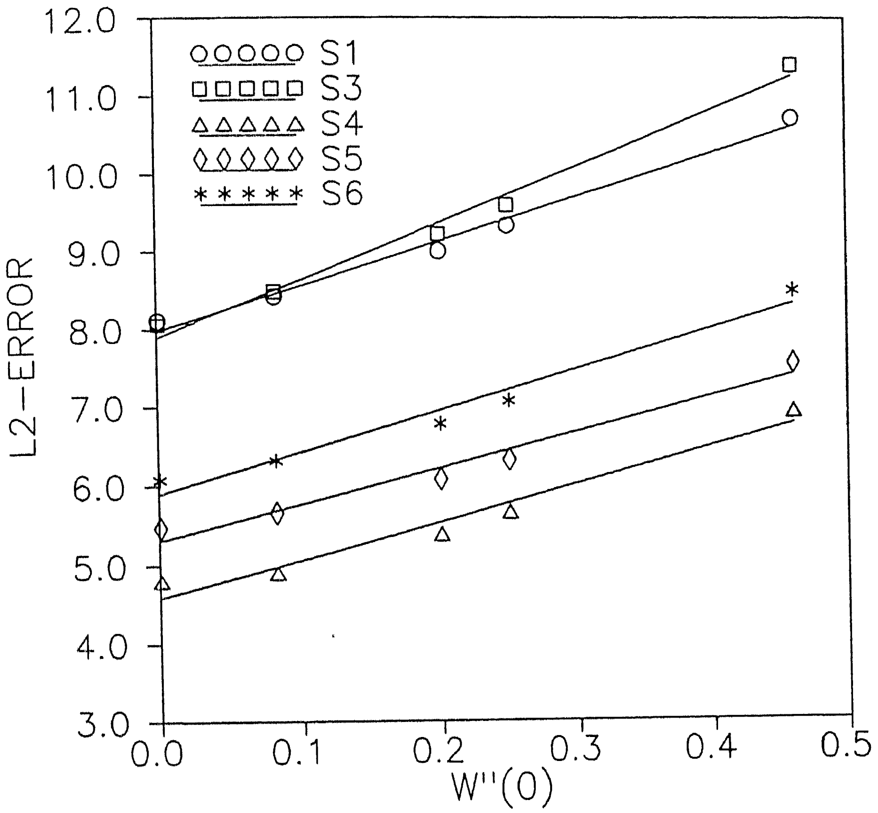

Fig. 7.1: Comparative performance (L−2 error) of filters for simulated sample

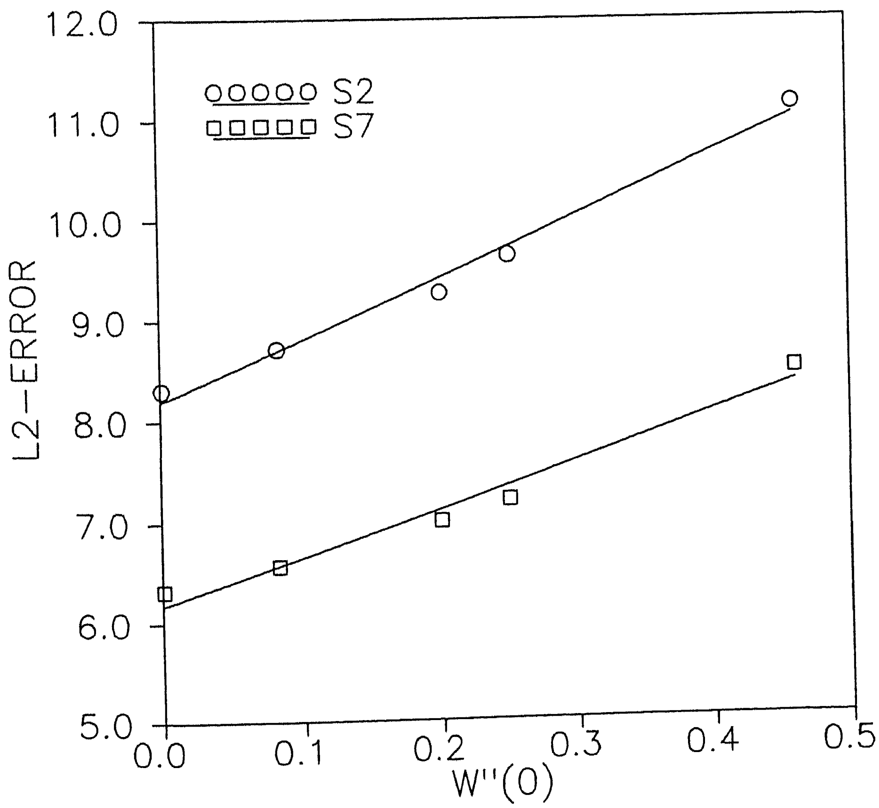

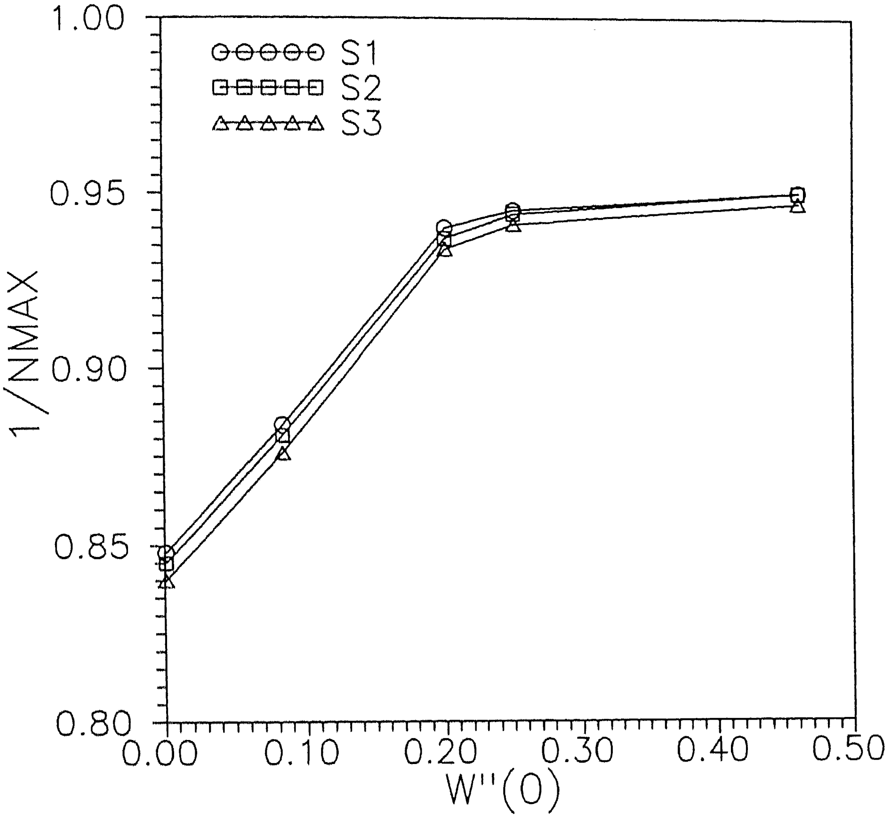

Fig. 7.3: Comparative performance (1/NMAX) of filters for simulated samples

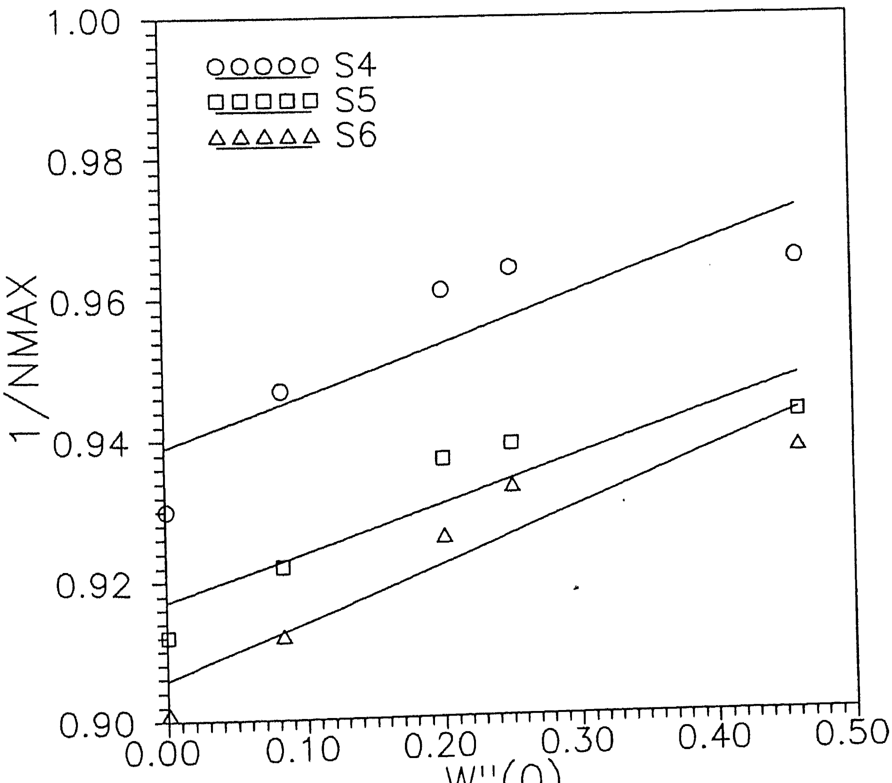

Fig. 7.4: Comparative performance (1/NMAX) of filters for simulated samples

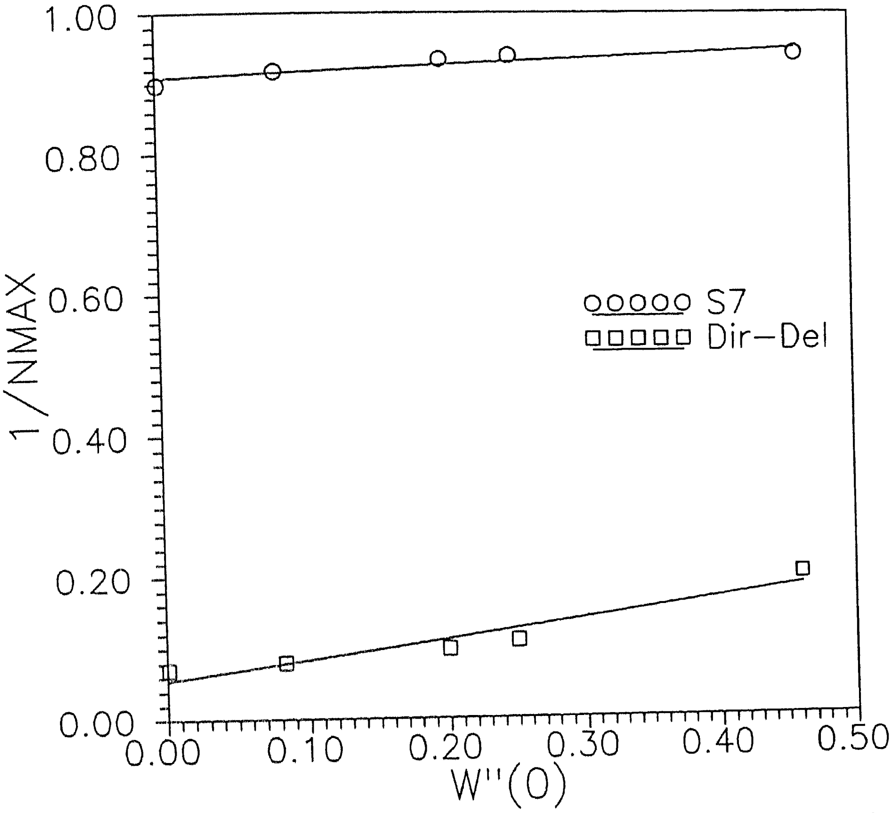

Fig.7.5: Comparative performance (1/NMAX) of filters for simulated sample

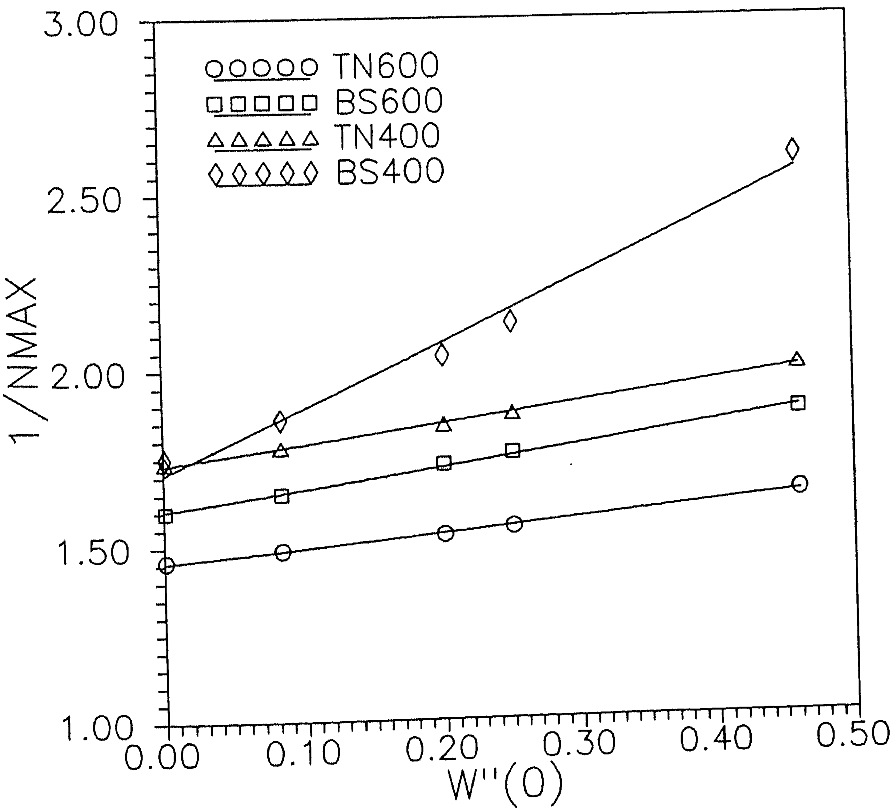

Fig. 7.6: Comparative performance (1/NMAX)of filters for two phase flow data

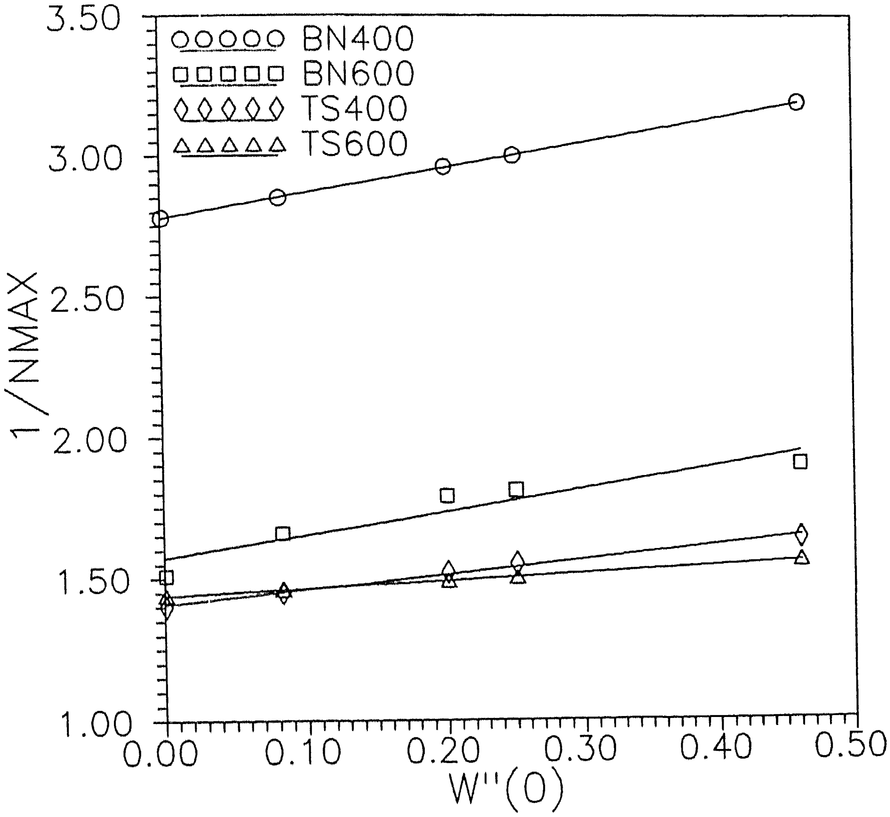

Fig. 7.7: Comparative performance (1/NMAX) of filters for two phase flow data

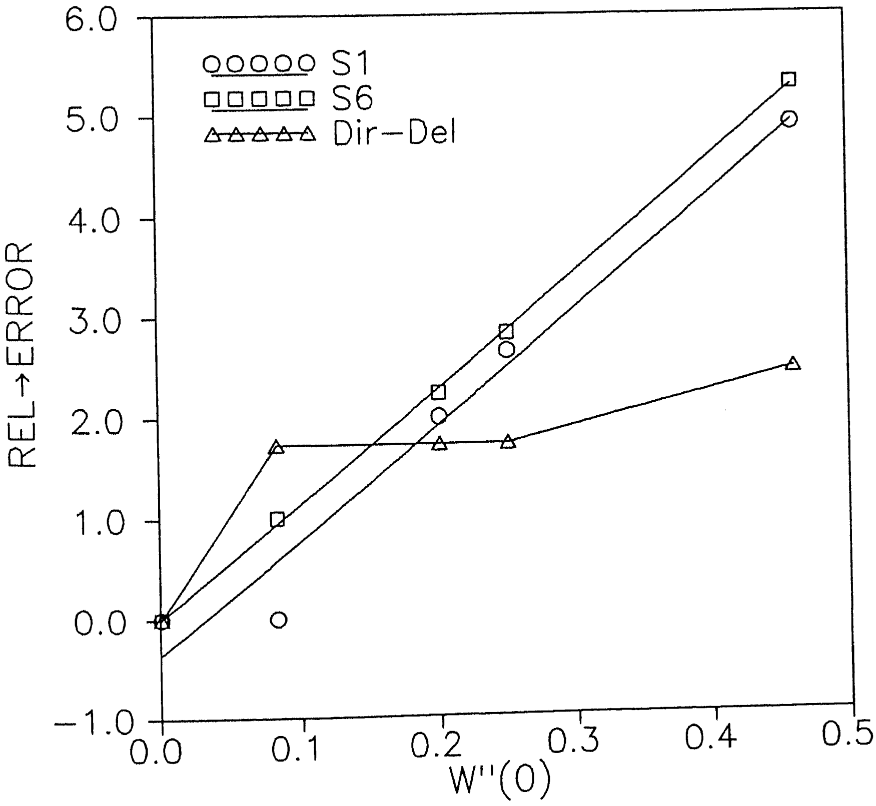

Fig. 7.8: Comparative performance (relative error) of filters for simulated samples

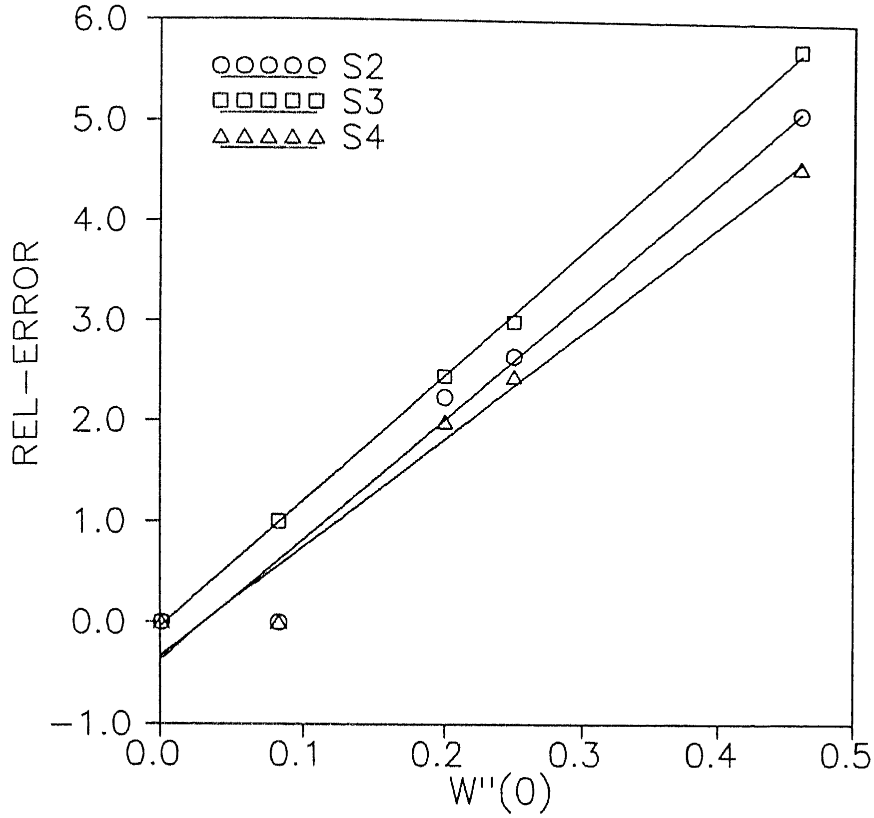

Fig. 7.9: Comparative performance (relative error) of filters for simulated samples

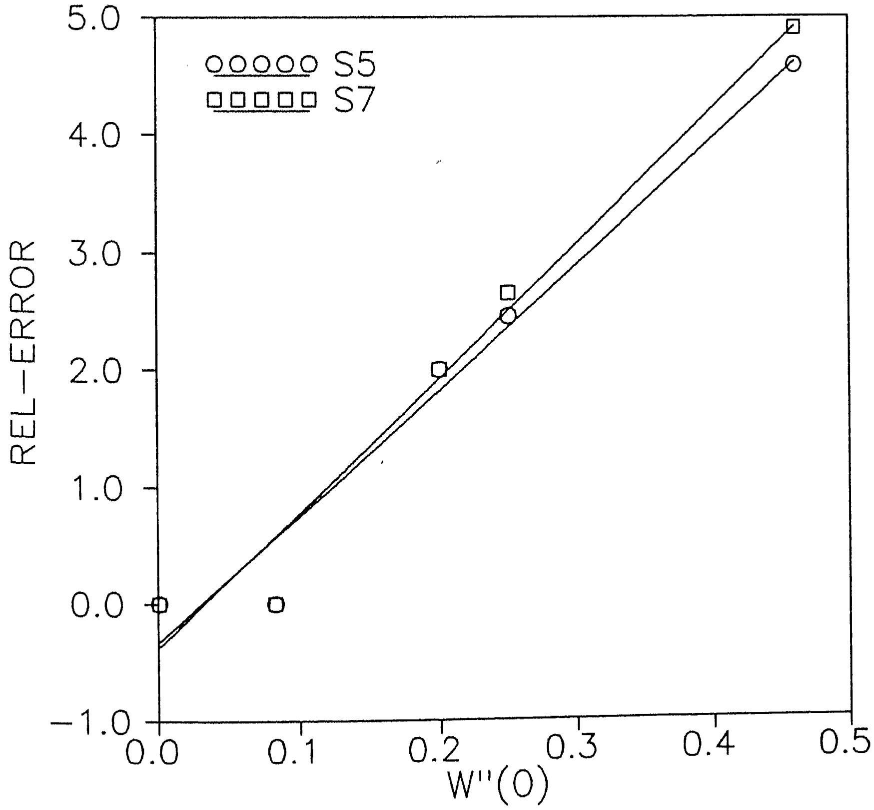

Fig. 7.10 Comparative performance (relative error) of filters for simulated samples

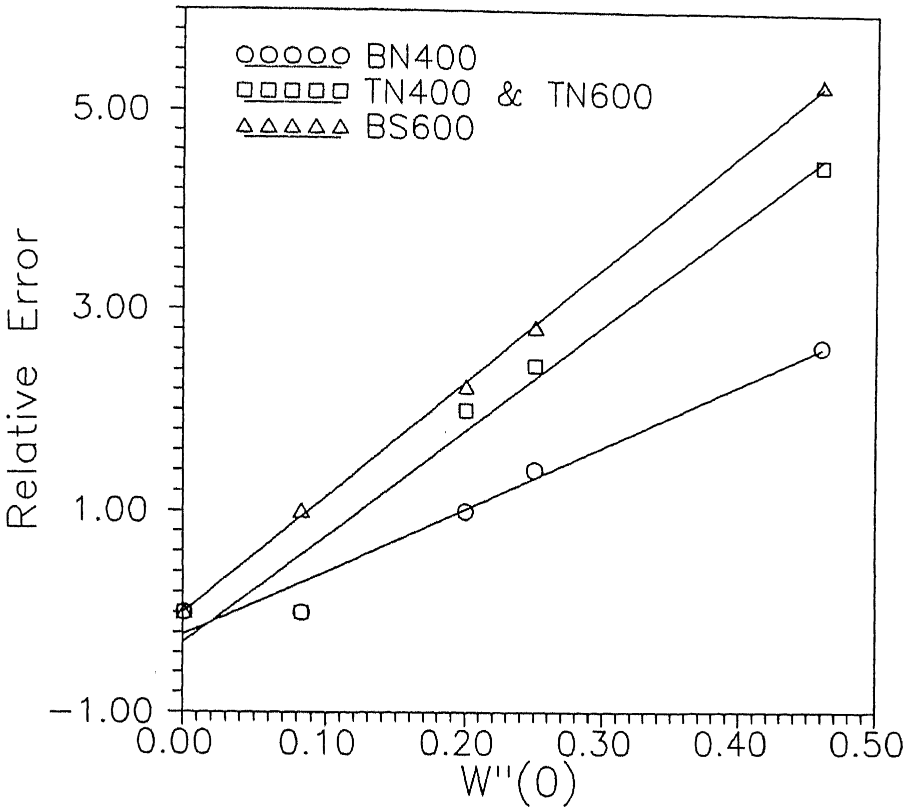

Fig. 7.11: Comparative performance (Relative Error) of filters for two phase flow

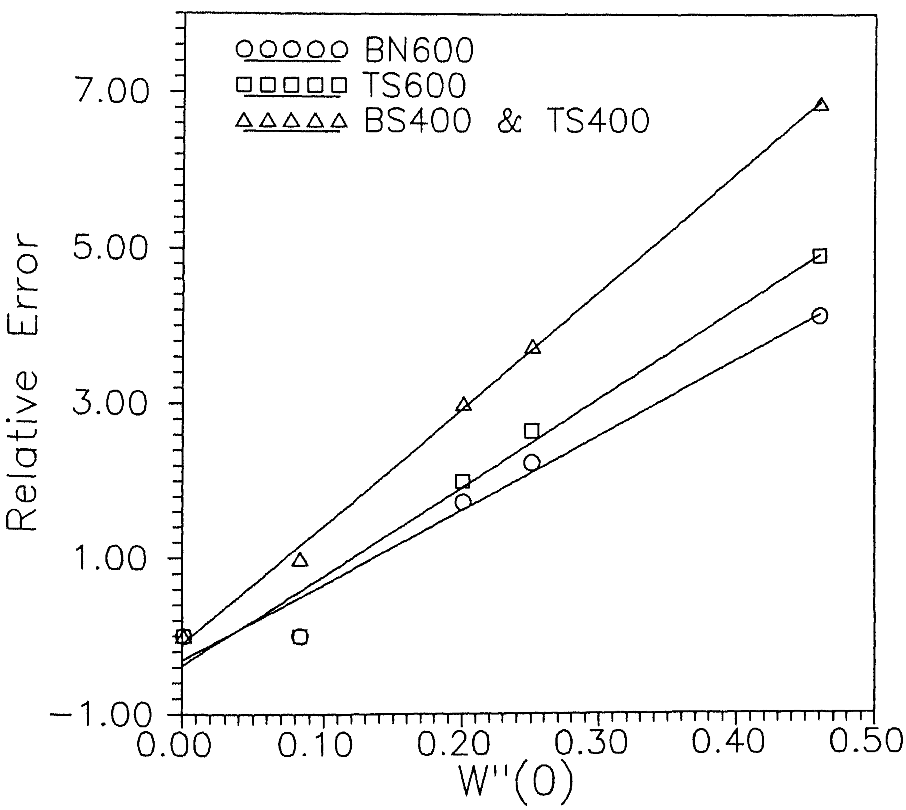

Fig. 7.12: Comparative performance (relative Error) of filter for two phase flow

Chapter 8

Conclusion

The findings of this study on liquid-metal magneto-hydrodynamic system are summarised below.

- This study clearly shows the lack of radial symmetry in the two phase flow system. Thus, more data has to be collected (from different angles) to do an accurate study of non-symmetry in the flow.

- The study done using filters on simulated as well as real (two-phase flow) data shows that the area averaged and centerline averaged values of linear absorption coefficient (or void-fraction) is very nearly the same, though, the NMAX values are quite different.

- The reconstruction results reported in chapter 6 are quite good in view of the linearity of the error graphs which are achieved only for perfect data conditions. The data of Jayakumar(1996) appears to be near "perfect". Thus an independent confirmation of the goodness of the data used has been established.

- For two-phase flow data, variance recorded for the error graph (showing 1/NMAX), are an order of magnitude smaller as compared to that for simulated data. This is because, in simulated geometries the function being uniform over a

large region, $\nabla^2 f$ vanishes, while for the two-phase flow system, the presence of a large number of bubbles $\nabla^2 f$ exists for the correspondimg mathematical distribution representing the mercury-nitrogen two-phase flow.

8.1 Scope for Further Work

- Flow being not symmetrical, needs to be studied in greater detail.

- Study to verify whether the flow has fully developed.

- Quantative study to correlate the pressure variation with height & flow rate.

- Use of fractals to represent error.

- Slip velocity can be computed to relate the relative velocity of mercury and nitrogen.

References

[1] Davis G.R., Munshi P., Elliot J.C., An analysis of biological hard tissues using the tomographic reconstruction error formula. *Journal of X-ray science and technology* 6(1996), pp 63-76.

[2] Herman G.T., *Image reconstructions from projections: The fundamentals of computerised tomography.* Academic Press, 1980.

[3] Jayakumar P., Munshi P., Satyamurthy P., Thiyagrajan T.K., Dixit N.S., Venkatramani, Non-invasive measurement of void-fraction profiles in a vertical mercury-nitrogen flow(in review).

[4] Jayakumar P., *Tomographic reconstruction of void-fraction profiles in a Mercury-Nitrogen flow system* M.Tech Thesis, Indian Institute of Technology, Kanpur(1996).

[5] Lewitt R.M., Reconstruction algorithms: Transform methods proceedings *IEEE* 71 No. 3(1983). pp 390-408.

[6] Munshi P., Maisal M., Reiter H., Experimental aspects of the approximate error formula for tomographic reconstruction, Tech. rep. TW93 *Fraunhofer Institute for NDT, Saarbruecken*(1993).

[7] Munshi P., Error analysis of tomographic filters I: Theory, *NDT & E International*, 25(1992), pp 191-194.

[8] Munshi P., Vaidya M. S., Void fraction reconstruction with stochastic data.*Experiments in fluids*, 16 (1994), pp 217-222.

[9] Natterer F., The mathematics of computerised tomography, *John Wiley and Sons, New-York*(1986).

[10] Satyamurthy P., Novel liquid metal mahneto-hydrodynamic electric power generators. *Physics Education*,10(1994), pp 398-409.

[11] Singh N.K., *Experimental transmission tomography Using gamma-rays.* M.Tech Thesis, Indian Institute of Technology, Kanpur(1995).

[12] Wells P.,Munshi P., An investigation of the theoretical error in tomographic images. *Nuclear instruments and methods in physics research* B 93(1994), pp 87-92.

Date Slip

This book is to be returned on the date last stamped.
